

**A semi-empirical method for estimating complete surface temperature from radiometric surface temperature, a study in Hong Kong city**

Yang, Jinxin; Wong, Man Sing; Ho, Hung Chak; Krayenhoff, E. Scott; Chan, P. W.; Abbas, Sawaid; Menenti, Massimo

**DOI**

[10.1016/j.rse.2019.111540](https://doi.org/10.1016/j.rse.2019.111540)

**Publication date**

2020

**Document Version**

Accepted author manuscript

**Published in**

Remote Sensing of Environment

**Citation (APA)**

Yang, J., Wong, M. S., Ho, H. C., Krayenhoff, E. S., Chan, P. W., Abbas, S., & Menenti, M. (2020). A semi-empirical method for estimating complete surface temperature from radiometric surface temperature, a study in Hong Kong city. *Remote Sensing of Environment*, 237, Article 111540. <https://doi.org/10.1016/j.rse.2019.111540>

**Important note**

To cite this publication, please use the final published version (if applicable). Please check the document version above.

**Copyright**

Other than for strictly personal use, it is not permitted to download, forward or distribute the text or part of it, without the consent of the author(s) and/or copyright holder(s), unless the work is under an open content license such as Creative Commons.

**Takedown policy**

Please contact us and provide details if you believe this document breaches copyrights. We will remove access to the work immediately and investigate your claim.

1 **A semi-empirical method for estimating complete surface temperature from**  
2 **radiometric surface temperature, a study in Hong Kong city**

3 Jinxin Yang<sup>1,2</sup>, Man Sing Wong<sup>2\*</sup>, Hung Chak Ho<sup>2,3</sup>, E. Scott Krayenhoff<sup>4</sup>, PW  
4 Chan<sup>5</sup>, Sawaid Abbas<sup>2</sup>, Massimo Menenti<sup>6,7</sup>

5 <sup>1</sup>School of Geographical Science, Guangzhou University, Guangzhou 510275, China,

6 yangjx11@gzhu.edu.cn

7 <sup>2</sup>Department of Land Surveying and Geo-Informatics, The Hong Kong Polytechnic

8 University, Kowloon, Hong Kong; email: lswong@polyu.edu.hk

9 <sup>3</sup>Department of Urban Planning and Design, The University of Hong Kong, Hong

10 Kong; hcho21@hku.hk

11 <sup>4</sup>School of Environmental Sciences, University of Guelph, Guelph, ON, Canada,

12 skrayenh@uoguelph.ca

13 <sup>5</sup>Hong Kong Observatory, Hong Kong, pwchan@hko.gov.hk

14 <sup>6</sup>Faculty of Civil Engineering and Earth Sciences, Delft University of Technology,

15 P. O. Box 5048, 2600 GA Delft, Netherlands; e-mail: m.menenti@tudelft.nl

16 <sup>7</sup>State Key Laboratory of Remote Sensing Science, Institute of Remote Sensing and

17 Digital Earth, Chinese Academy of Sciences, Beijing 100101, PR China

18

- 19 SYMBOLS and ACRONYMS:
- 20  $T_c$  - complete surface temperature (K)
- 21  $T_r$  - radiometric temperature from nadir view direction (K)
- 22 TUF-3D - Temperatures of Urban Facets in 3D
- 23  $\lambda_p$  - planar area index
- 24  $F$  - wall facet area index
- 25 ASTER - Advanced Spaceborne Thermal Emission and Reflection Radiometer
- 26 TM - Landsat Thematic Mapper
- 27 UST - urban surface temperature (K)
- 28 LASER/F-LAent, SEnsible, Radiation Fluxes
- 29  $Kn$  - solar radiation above urban canopy ( $W/m^2$ )
- 30  $\theta_a$  - solar azimuth angle ( $^\circ$ )
- 31  $\theta_z$  - solar zenith angle ( $^\circ$ )
- 32  $T_{roof}$  - roof temperature (K)
- 33  $T_{road}$  - road temperature (K)
- 34  $T_{wall}$  - wall temperature (K)
- 35  $L_r$  - radiation at the bottom of atmosphere at nadir view modeled by TUF-3D ( $W/m^2$ )
- 36  $\varepsilon$  - emissivity
- 37  $\sigma$  - Stefan–Boltzmann constant ( $5.6703 \times 10^{-8} W m^{-2} K^{-4}$ )
- 38  $L_d$  - downwelling atmospheric radiation
- 39  $E(i)$  - radiance leaving urban canopy of pixel  $i$  ( $W \cdot m^{-2} \cdot sr^{-1} \cdot \mu m^{-1}$ )
- 40  $R_{at\uparrow}$  - downward atmospheric thermal radiance ( $W \cdot m^{-2} \cdot sr^{-1} \cdot \mu m^{-1}$ )

41 **Abstract**

42 The complete surface temperature ( $T_c$ ) in urban areas, defined as the mean  
43 temperature of the total active surface area, is an important variable in urban micro-  
44 climate research, specifically for assessment of the urban surface energy balance.  
45 Since most vertically-oriented building facets are not observed by a nadir-viewing  
46 remote imaging radiometer, the radiometric surface temperature ( $T_r$ ) measured at a  
47 specific view angle cannot be used with existing heat transfer equations to estimate  
48 radiative and convective fluxes in the urban environment. Thus, it is necessary to  
49 derive  $T_c$  for city neighborhoods. This study develops a simple method to estimate  $T_c$   
50 from  $T_r$  with the aid of the Temperatures of Urban Facets in 3D (TUF-3D) numerical  
51 model, which calculates 3-D sub-facet scale urban surface temperatures for a variety  
52 of surface geometries and properties, weather conditions and solar angles. The effects  
53 of geometric and meteorological characteristics – e.g., building planar area index ( $\lambda_p$ ),  
54 wall facet area index ( $F$ ), solar irradiance – on the difference between  $T_c$  and  $T_r$  were  
55 evaluated using the TUF-3D model. Results showed the effects of geometric and  
56 meteorological characteristics on the difference between  $T_c$  and  $T_r$  differ between  
57 daytime and nighttime. The study then sought to predict the relationship between  $T_r$   
58 and  $T_c$ , using  $\lambda_p$ ,  $F$ , and solar irradiance for daytime and only using  $\lambda_p$  and  $F$  for  
59 nighttime. Based on the simulated data from TUF-3D, the resulting relationships  
60 achieve a coefficient of determination ( $r^2$ ) of 0.97 and a RMSE of 1.5 K during  
61 daytime, with corresponding nighttime values of  $r^2 = 0.98$  and RMSE = 0.69 K. The  
62 relationships between  $T_r$  and  $T_c$  are evaluated using high resolution airborne thermal

63 images of daytime urban scenes:  $r^2 = 0.75$  and RMSE = 1.09 K on August 6, 2013 at  
64 12:40 pm; and  $r^2 = 0.86$  and RMSE = 1.86K on October 24, 2017 at 11:30 am. The  
65 new relationships were also applied to estimate  $T_c$  from  $T_r$  in Hong Kong retrieved  
66 from Landsat 5 Thematic Mapper (TM) and the Advanced Spaceborne Thermal  
67 Emission and Reflection Radiometer (ASTER). In the present climatic context, the  
68 difference between  $T_c$  and  $T_r$  can reach 10 K during daytime in summer, and 6 K  
69 during daytime in winter, with seasonal variation attributable to the variations in  
70 shortwave irradiance. The nighttime difference between  $T_c$  and  $T_r$  can also reach 2 K  
71 in both summer and spring seasons.

72 **Keywords:** remote sensing, surface temperature, thermal heterogeneity, urban  
73 geometry

## 74 **1. Introduction**

75 Background. Urban Surface Temperature (UST) is a key variable for studying  
76 urban surface energy exchange and microclimate in an urban environment (Arnfield,  
77 2003; Arnfield and Grimmond, 1998; Cheng et al., 2010; Morrison et al., 2018;  
78 Nazarian et al., 2018a; Oke, 1988; Voogt and Oke, 2003; Yaghoobian et al., 2010).  
79 Satellite-based thermal infrared (TIR) data have been used for studying urban surface  
80 temperature and provide information at different temporal and spatial scales (Li et al.,  
81 2013), thus surface temperature from remote sensing data has been widely applied in  
82 urban climate research (Dousset and Gourmelon, 2003; Roth et al., 1989; Voogt and  
83 Oke, 2003; Weng, 2009). Most space-borne imaging radiometers observe terrestrial

84 targets in a close to nadir view direction and, therefore, can capture only horizontal  
85 facets. Thus, active radiation sources would be incompletely observed over urban  
86 areas (Adderley et al., 2015; Jiang et al., 2018; Roth et al., 1989). Theoretically, off-  
87 nadir-view satellite sensors can observe the vertical walls, but only a few multi-angle  
88 sensors provide off-nadir image data with thermal infrared spectral range, and such  
89 satellite images (e.g. Sea and Land Surface Temperature Radiometer (SLSTR) on-  
90 board Sentinel 3, ATSR-series) are with low spatial resolution (1km), which is not  
91 capable to be used over high-density urban environment. For densely built areas,  
92 active radiation sources are much larger than the horizontal area due to the large  
93 surface area of vertical facets (Roth et al. 1989). It is therefore challenging to retrieve  
94 urban surface temperature accurately and without large bias using thermal infrared  
95 remote sensing (Jiang et al., 2018).

96 In terms of the urban energy balance, convective heat transfer is often influenced  
97 by the complete surface of each roughness element. Thus, a representative surface  
98 temperature of the complete and 3D surface-atmosphere interface should be estimated  
99 since these temperatures contribute to the local heat exchange (Kanda et al., 2007;  
100 Kanda et al., 2005; Voogt and Oke, 1997). Voogt and Oke (1997) proposed the  
101 concept of the complete urban surface temperature ( $T_c$ ), defined as weighted  
102 summation of the component surface temperatures, multiplied by the associated  
103 component fractions from a three-dimensional perspective. Compared with the  
104 radiometric surface temperature directly captured by a nadir-viewing remote imaging  
105 radiometer,  $T_c$  can provide superior information towards understanding urban climate.

106 Voogt and Oke (1997) compared sensible heat fluxes calculated from air temperature  
107 and different surface temperatures, and their results showed that the complete surface  
108 temperature should be used for the estimation of sensible heat flux in urban areas. In  
109 order to consider its significant implications in urban climate research, researchers  
110 have attempted to calculate  $T_c$  from remote sensing or field measurements (Allen et  
111 al., 2018; Jiang et al., 2018; Voogt and Oke, 1997). Voogt and Oke (1997) calculated  
112  $T_c$  based on field measurement by a thermal camera data and digitizing building data  
113 from high-resolution (1:2500) aerial photography. Their results showed that there is a  
114 significant difference between  $T_c$  and the nadir  $T_r$ . Allen et al. (2018) calculated  $T_c$   
115 from the hemispherical  $T_r$  measured by pyrometers and results showed that the  
116 difference between  $T_c$  and the temperature observed from a nadir view is up to 8 K  
117 under clear-sky viewing conditions. Jiang et al. (2018) estimated  $T_c$  from directional  
118 radiometric temperature based on simulated data from urban micro-climate model and  
119 remote sensing observation model, without ancillary ground-based data. They  
120 indicated that the estimation of  $T_c$  could be further improved by using radiometric  
121 temperatures observed at multiple view-angles.

122 Gaps in knowledge. The aforementioned studies estimated the  $T_c$  using field  
123 measurements or airborne data, while the estimation of  $T_c$  from satellite remote  
124 sensing data is still challenging due to their relatively low spatial resolution and to the  
125 thermal heterogeneity within the mixed pixels, which include roof and road facets  
126 with different temperatures. Since radiometric temperature is more readily available  
127 from satellite images than  $T_c$ , this study proposes a simple method to estimate  $T_c$  from

128 nadir observations of radiometric temperature view ( $T_r$ ). A nadir viewing imaging  
129 radiometer can only observe the radiance emitted by horizontal facets and reflected by  
130 horizontal facets from facets around and atmosphere. The temperature of horizontal  
131 facets is also affected by vertical walls due to the radiative transfer and energy  
132 exchange between vertical walls and road surfaces (Nazarian and Kleissl, 2015; Yang  
133 and Li, 2015). Thus,  $T_r$  is related to wall temperatures and related to  $T_c$  to some  
134 extent.  $T_r$  and  $T_c$  are correlated with the building height, density of building, material  
135 and local climatic conditions. Buildings in a city have influences on the radiative and  
136 convective transfer and imply energy exchange of the wall facets with ambient  
137 atmosphere, which results in the spatial variability of urban surface temperature. In  
138 addition, shadows cast by buildings affect the variability of surface temperatures. For  
139 homogeneous or “pure” pixels,  $T_r$  and  $T_c$  are more or less identical, while thermally  
140 heterogeneous pixels in urban spaces are always affected by the complexity of urban  
141 surfaces, including building density, aspect ratio (ratio of building height to the street  
142 width), and material properties which contribute differently to energy exchange. Thus,  
143 the relationships between  $T_r$  and  $T_c$  can be parameterized by urban structural  
144 parameters (e.g. building density, building height) and local meteorological  
145 parameters. In order to develop the relationships, complex energy exchange within  
146 mixed pixels with high heterogeneity of urban surface temperature should be  
147 modeled.

148 The Temperatures of Urban Facets in 3D (TUF-3D) numerical model was  
149 adopted and used in this study to simulate  $T_r$  and  $T_c$  (Krayenhoff and Voogt, 2007).



150 TUF-3D provides (sub-) facet surface temperatures based on sub-facet scale solutions  
151 to the surface energy balance. The  $T_c$  can also be calculated therefore, by combining  
152 the facet surface temperatures provided by TUF-3D with the associated facet areas.  $T_r$   
153 is provided by TUF-3D in order to represent a sensor viewing from a nadir direction,  
154 and it is calculated from the radiation emitted and reflected by roofs and roads.

155 Objectives. In order to estimate  $T_c$  from  $T_r$ , this study explored and established a  
156 relationship between  $T_c$  and  $T_r$  in a thermally heterogeneous environment with the use  
157 of numerical experiments based on TUF-3D and urban building structure parameters  
158 (Planar Area Index ( $\lambda_p$ ) and Wall Facet area index ( $F$ )). The objectives of this study  
159 were 1) to assess the effects of urban building geometric parameters (e.g.  $\lambda_p$ ,  $F$ ) and  
160 local meteorological conditions (e.g. wind speed, solar radiation) on the relationship  
161 between  $T_c$  and  $T_r$ ; and 2) to evaluate the relationship between  $T_c$  and  $T_r$  using an  
162 urban energy balance model and numerical experiments and develop a simple method  
163 that uses  $T_r$  to retrieve  $T_c$  in a thermally heterogeneous urban environment.  
164 Subsequently, the developed method is used to estimate  $T_c$  from radiometric surface  
165 temperature observed by satellite data of the Landsat 5 Thematic Mapper (TM) with  
166 30 m spatial resolution in daytime and Advanced Spaceborne Thermal Emission and  
167 Reflection Radiometer (ASTER) with 90 m spatial resolution in nighttime.

168 The study is organized as follows. After an Introduction structured in two sub-  
169 sections to articulate our problem statement, the objectives are stated, followed by a  
170 detailed presentation of the Methodology structured in five sub – sections, to describe

171 separately a sensitivity analysis and the design of numerical experiments from the  
172 development of a simple model to estimate  $T_c$  from  $T_r$ . Next, the data applied in the  
173 study are described by type, i.e. radiometric data acquired by satellites, digital surface  
174 models and meteorological data. The presentation of results mirrors the structure of  
175 the Methodology and is followed by a detailed Discussion. Lastly, the section of  
176 Conclusions is presented.

## 177 **2. Methodology**

### 178 **2.1 General**

179 In this study, a simple method is developed to estimate the complete surface  
180 temperature  $T_c$  from remote sensing measurements of the radiometric surface  
181 temperature  $T_r$  for daytime and nighttime respectively. For daytime, the method is  
182 based on a relationship  $f_a$ :

$$183 \quad T_c = f_a(T_r, \lambda_p, F, Kn, \theta_a, \theta_z) \quad (1)$$

184 where  $T_r$  is the nadir radiometric temperature (K),  $\lambda_p$  is the planar area index,  $F$  is the  
185 wall facet area index,  $Kn$  is the down-welling solar irradiance at the top of the urban  
186 canopy ( $\text{W/m}^2$ ),  $\theta_a$  is the solar azimuth angle ( $^\circ$ ), and  $\theta_z$  is the solar zenith angle  
187 ( $^\circ$ ).  $\lambda_p$ , defined as the ratio of plan area of buildings to the area of building footprint, is  
188 related to the building density. Specifically,  $\lambda_p$  is defined as the ratio of building total  
189 planar area to the area of the horizontal plane section of the building at ground level.  
190 The building footprint is the area of the horizontal plane section of the building at

191 ground level. The wall facet area index ( $F$ ), calculated as the ratio of the wall facet  
192 area to the area of building footprint which contains the building and the road around  
193 it, is related to the building density and aspect ratio.  $\lambda_p$  is related to the directional  
194 temperature observed by remote sensing from nadir direction.  $F$  is related to the  
195 fraction unobserved by remote sensing. Thus,  $F$  and  $\lambda_p$  were used in this study as the  
196 building structure parameters to study the difference between  $T_c$  and  $T_r$ .

197 Fewer variables and parameters are taken into account during nighttime since the  
198 solar effects can be neglected at nighttime and the relationship between  $T_c$  and  $T_r$   
199 becomes:

$$200 \quad T_c = f_n(T_r, \lambda_p, F) \quad (2)$$

201 To construct our simple model, we used a large number of numerical experiments  
202 (see Sect. 2.3 for details) by TUF 3D (Krayenhoff and Voogt, 2007) to generate the  
203 pseudo – observations required to determine the relationships Eq.1 and 2.  
204 Considering that the solar effects would continue about 3 hours after sunset, the  
205 daytime numerical experiments from 8:00 am until 5:00 pm and the nighttime  
206 numerical experiments from 9:00 pm until 5:00 am were used for studying the  
207 relationships in Eqs. 1 and 2 between  $T_c$  and  $T_r$ .

208 Our study was limited to the built-up area where the fractional abundance of  
209 vegetation is negligible, so that the temperature of vegetation is not considered in this  
210 study. This is also aligned with our estimation in the TUF-3D model. The  $T_c$  was  
211 calculated using the facet temperatures (roof temperature  $T_{roof}$ , road temperature

212  $T_{road}$  and wall temperature  $T_{wall}$ ) and the facet area weights extracted from the TUF-  
213 3D output:

$$214 \quad T_c = \frac{T_{roof} * \lambda_p + T_{road} * (1 - \lambda_p) + T_{wall} * F}{1 + F} \quad (3)$$

215  $T_r$  was calculated from the area-weighted average of upwelling radiation from  
216 roof and road facets according to the definition given by (Becker and Li, 1995). Since  
217 satellite sensors have narrow fields of view, only the roof and road facets are observed  
218 from a nadir view. The upwelling radiation includes the emitted radiation by roof and  
219 road facet and the radiation emitted by wall facets and atmosphere, then reflected by  
220 roof and road facets. The reflected radiation depends on the wall surface temperature  
221 and material emissivities of walls and roads as well as the sensor-ground geometry. In  
222 this study, we only consider the nadir radiometric temperature. In the TUF – 3D  
223 domain, we obtained the  $T_r$  from the radiation at the bottom of atmosphere  $L_r$   
224 captured by the pseudo – observations collected by a fictive nadir – viewing imaging  
225 radiometer placed:

$$L_r = \varepsilon \sigma T_r^4 + (1 - \varepsilon) L_d \quad (4)$$

226  $\varepsilon$  is calculated as the area-weighted average of roof and road emissivities.  $\sigma$  is the  
227 Stefan–Boltzmann constant ( $5.6703 \times 10^{-8} \text{ Wm}^{-2}\text{K}^{-4}$ ).  $L_d$  is the downwelling  
228 atmospheric radiation,  $T_r$  is the radiometric temperature measured by a fictive nadir-  
229 viewing remote radiometer. The TUF-3D provides the upwelling radiation from  
230 road and roof which includes the radiation emitted by roof and road facets and the  
231 radiation emitted by wall facets and by the atmosphere and reflected by roof and road  
232 facets. Then the  $L_r$  can be calculated as the area weighted average of roof and road  
233 facets.  $L_d$  is calculated from the atmospheric profile in TUF-3D.

234 The design of the numerical experiments is described in Sect. 2.3. The variables

235 and parameters in the Eq.1 and Eq. 2 (e.g.  $\lambda_p, F, Kn, \theta_a, \theta_z$ ) may have different  
236 influence on the relationship between  $T_c$  and  $T_r$ . The approach to evaluate how  
237 influential such variables and parameters are, is explained in Sect. 2.4. Finally, the  
238 relationships in Eq.1 and Eq.2 were determined and evaluated as described in Sect.  
239 2.5.and 2.6.

## 240 2.2 Overview of the TUF-3D model

241 TUF-3D is a micro-scale urban energy balance model that represents the three-  
242 dimensional (3D) energy exchange in response to meteorological forcing, i.e. solar  
243 irradiance, wind speed and air temperature. The energy fluxes and (sub-) facet  
244 surface temperatures calculated with this model have been validated with  
245 measurements (Krayenhoff and Voogt, 2007). TUF-3D has also been used to estimate  
246 UST of heterogeneous pixels from the facet surface temperatures (Krayenhoff and  
247 Voogt, 2016), as well as to evaluate radiation models (Krayenhoff et al., 2014). TUF-  
248 3D describes sensible heat transfer in a simplified way by assuming that a constant  
249 flux layer extends to the surface, wherein the vertical profiles of wind speed and  
250 temperature are logarithmic (Krayenhoff and Voogt, 2007). This assumption can  
251 reduce computational costs in view of modeling large neighborhood or entire cities.  
252 In reality, heat transfer is complex because of the coherent turbulent structures and  
253 the complexity of the urban canopy layer due to the complex urban morphology and  
254 heterogeneous urban facets(Grimmond et al., 2011; Grimmond et al., 2010; Wang et  
255 al., 2014).The hypothesis of logarithmic vertical profiles of wind speed and air

256 temperature is widely adopted in urban micro-climate models, e.g. LASER/F  
257 (LATent, SEnsible, Radiation Fluxes) (Kastendeuch and Najjar, 2009; Kastendeuch et  
258 al., 2017). Lee et al. (2013) applied LASER/F to generate synthetic, high-resolution  
259 thermal images of building facets and evaluated the impact of the simplified  
260 description of momentum and heat transfer in LASEF/F by comparing it with a  
261 Computational Fluid Dynamics (CFD) model. The results showed that the impact on  
262 facet energy balance and surface temperature was relatively small. Accordingly, we  
263 accepted the hypothesis of logarithmic profiles in the urban canopy layer in TUF-3D.

### 264 **2.3 Design of numerical experiments**

265 Urban geometric parameters, including building planar area index ( $\lambda_p$ ) and aspect  
266 ratio, and local meteorological conditions, including wind speed and solar radiation,  
267 have a direct impact on the relationship between  $T_c$  and  $T_r$ . To study the influence of  
268 these variables and parameters on the difference between  $T_c$  and  $T_r$ , several numerical  
269 experiments for different values of  $\lambda_p$  and aspect ratio under different meteorological  
270 conditions were carried out. The total number of numerical experiments is limited by  
271 available computational resources, so we limited the number of levels applied for  
272 each variable and parameter. According to Stewart et al. (2014),  $\lambda_p$  ranges from 0.1 to  
273 0.90 and aspect ratio ranges between 0.1 and more than 2.5 for typical urban local  
274 climate zones. The  $\lambda_p$  ranges from 0.1 to 0.70 in this study because of the computing  
275 ability. Aspect ratio is calculated as the ratio of building height to street width. In  
276 TUF-3D,  $\lambda_p$  and ratio of building height to length (H/L) can be used to replace the

277 aspect ratio. In the TUF-3D, a building has a square horizontal section. The building  
 278 length is equal to the building width of the building roof or base. The meteorological  
 279 data, including solar radiation, wind speed, air temperature, air pressure, on cloudless  
 280 days of each month from the Hong Kong Observatory were selected as input (Table  
 281 1).

282 Table 1. Surface building geometries and dates of meteorological parameters used  
 283 in TUF-3D

$\lambda_p$	H/L	Dates of meteorological parameters (solar radiation, wind speed, air temperature, air pressure)
0.1-0.7	0.5-5.5	Feb 27 2010, Mar 10 2010, Apr 11 2010, May 25 2010, Jul 1 2010, Aug 2 2010, Sept 17 2010, Oct 28 2010, Nov 27 2010, Dec 7 2010

284

285 The values of thermal and radiative parameters of urban materials adopted in this  
 286 study were also based on Stewart et al. (2014) and explore a broad range of  
 287 conditions, so that the results of the analysis apply to a range of different urban  
 288 conditions, e.g. from high-rise compacted city to open low-rise city space. The  
 289 material properties in real world are complex, the values used in this study can  
 290 represent the typical condition of the real world (Stewart et al., 2014). The material  
 291 emissivity spectra of rooftop, wall facet and road were applied to estimate the  
 292 emissivities in the Landsat 5 TM and ASTER spectral bands (Table 2). The material  
 293 emissivity is calculated from the urban material spectral library (Kotthaus et al., 2014)  
 294 and the satellite spectral response functions used in this study. We assume that roof is

295 constructed by concrete and brick, and the material emissivity of roof is the average  
296 value of concrete and brick. The road is constructed by the concrete and asphalt and  
297 the material emissivity of road is the average value of concrete and asphalt.

298 The geometric and meteorological parameters in Table 1 were combined with thermal  
299 and radiative material properties in Table 2 to carry out the numerical experiments  
300 with TUF 3D. In total about 17000 sets of data were carried out. Subsets of the results  
301 were used in the sensitivity analysis described in Sect. 2.4, while the results of all  
302 experiments were combined to determine our simple model (Sect. 2.5).



303

304

Table 2. Thermal and radiative properties used in TUF-3D (Stewart et al., 2014)

Surface properties	Group 1	Group 2	Group 3	Group 4	Group 5	Group 6	Group 7	Group 8	Group 9	Group 10
Emissivity:										
roof	0.937	0.945	0.937	0.945	0.937	0.945	0.937	0.945	0.937	0.945
wall	0.956	0.886	0.956	0.886	0.956	0.886	0.956	0.886	0.956	0.886
ground	0.956	0.948	0.956	0.948	0.956	0.948	0.956	0.948	0.956	0.948
Albedo:										
roof	0.13	0.18	0.15	0.13	0.13	0.13	0.13	0.18	0.13	0.1
wall	0.25	0.2	0.2	0.25	0.25	0.2	0.2	0.25	0.25	0.2
ground	0.15	0.16	0.18	0.2	0.2	0.24	0.24	0.17	0.23	0.21
thermal conductivity(W/m/K) :										
roof	1.4									
wall	1.12									
ground	0.84									
volumetric heat capacity ( $10^6$ J/m <sup>3</sup> /K):										
roof	1.61	1.61	1.02	1.60	1.60	1.02	2.85	1.60	1.03	2.85
wall	1.75	3.57	2.28	2.58	2.58	2.28	0.32	2.01	2.29	2.01
ground	1.59	1.45	1.33	1.17	1.10	1.04	0.84	1.42	0.89	1.08

305 **2.4 Evaluation of influential urban properties**

306 Synthetic data on  $T_c$  and  $T_r$  were generated with TUF-3D and used as pseudo-  
307 observations to construct relationships between  $T_c$  and  $T_r$  (see Sect.2.5). Prior to that, we  
308 have evaluated the influence of urban properties on the relation between  $T_c$  and  $T_r$  as  
309 described in this Section.

310 The urban geometric parameters,  $\lambda_p$  and  $F$ , were used to represent the urban geometric  
311 characteristics and further study the relationship between  $T_r$  and  $T_c$ . The wind speed ( $w$ )  
312 in TUF-3D is set at above canopy height, estimated as twice the building height. Wind  
313 has different effects on roof and ground surface temperature and these effects depend on  
314 building density and aspect ratio (Nazarian and Kleissl, 2015). Daytime  $T_c$  can be written  
315 as a function of  $T_r$ , urban geometry, solar irradiance and solar position. The sensitivity of  
316  $T_c$  to urban variables and parameters was evaluated by determining several different  
317 regressions, as listed in Table 3. The sensitivity analysis in Table 3 determines how the  
318 different variables affect the difference between  $T_c$  and  $T_r$  and which kind of equations  
319 should be constructed to estimate  $T_c$ .

320 Table 3 Sensitivity analysis of Eq.1. (the column of “specific sensitivity” describes each  
321 component of the sensitivity analysis by listing first the independent variables, then the  
322 variables taken as dependent; the column of “variables” lists the variables involved in the  
323 component sensitivity analysis; the column of “purposes” explains the objective of each  
324 component sensitivity analysis).

Specific sensitivity	Variables	Purposes
$T_c - T_r$ to $\lambda_p$	$T_c, T_r, \lambda_p$	How $\lambda_p$ affects the difference $T_c$ and $T_r$ and what kind of relationship

		exists between $T_c$ and $\lambda_p$
$T_c - T_r$ to $F$	$T_c, T_r, F$	How $F$ affects the difference between $T_c$ and $T_r$ and what kind of relationship exists between $T_c$ and $F$
$T_c - T_r$ to $Kn, \theta_a, \theta_z$	$T_c, T_r, Kn, \theta_a, \theta_z$	How solar parameters affect the difference between $T_c$ and $T_r$ and what kind of relationship exists between $T_c$ and solar parameters
$T_c - T_r$ to wind speed ( $w$ )	$T_c, T_r, w$	How wind speed affects the $T_c$ and $T_r$ and what kind of relationship exists between $T_c$ and wind speed
$T_c - T_r$ to material variations	$T_c, T_r$ , material properties in Table 2	How different material properties affect the difference between $T_c$ and $T_r$

325

## 326 2.5 Evaluation of the relationship between $T_c$ and $T_r$

327 Determination of the relationship between  $T_c$  and  $T_r$ . The relative weight of variables  
328 and parameters is evaluated by the sensitivity analysis described in Sect.2.4, which also  
329 indicates which kind of relationship, e.g. linear, exists between  $T_c - T_r$  and urban  
330 geometry parameters and climate variables. This can explain how urban geometry  
331 parameters and climate variables affect the difference between  $T_c$  and  $T_r$  and help to  
332 determine which kind of relationship between  $T_c$  and geometric/climate variables can be  
333 constructed. In Sect.2.4, the sensitivity analysis shows which parameters and variables  
334 are influential on  $T_c$  and which kind of relationship exists between  $T_c$  and these  
335 parameters.

336 In this section, the modelled  $T_c$  and  $T_r$  from TUF-3D were used to determine the  
337 relationship between  $T_c$  and  $T_r$ . According to the sensitivity analysis in Sect. 2.4, we  
338 included the following variables,  $\lambda_p, F, Kn, \theta_a, \theta_z$ , in the relationship to estimate  $T_c$

339 from  $T_r$  in daytime (Eq.5) and included variables  $\lambda_p$  and  $F$  in the relationship to estimate  
340  $T_c$  from  $T_r$  in nighttime (Eq.6). The relation between  $F$  and  $T_c$  is logarithmic according  
341 to the sensitivity analysis in Sect 2.4. The relationships between other variables and  $T_c$   
342 are linear. About 6700 sets of  $T_c$  and  $T_r$  modelled by TUF-3D were used to regress the  
343 coefficients of Eq. 5 to estimate  $T_c$  from  $T_r$  in daytime. About 6500 sets of  $T_c$  and  $T_r$   
344 modelled by TUF-3D under different structure and meteorological conditions in  
345 nighttime were used to regress the coefficients of Eq.6 to estimate  $T_c$  from  $T_r$  for the  
346 nighttime case. In both cases, the relationships are generic, in the sense that they apply to  
347 all cases explored by the numerical experiments. The accuracy of such parameterization  
348 of  $T_c$  is likely to increase when more predictive variables are applied. Since the  
349 sensitivity analysis suggests that a linear regression is sufficiently accurate, we  
350 determined the daytime parameterization of  $T_c$  as a multi-linear polynomial of the form:

$$351 \quad T_c = a_1 * T_r + a_2 * \lambda_p + a_3 * \ln F + a_4 * K_n + a_5 * \theta_a + a_6 * \theta_z + a_0 \quad (5)$$

352 and nighttime:

$$353 \quad T_c = b_1 * T_r + b_2 * \lambda_p + b_3 * \ln(F) + b_0 \quad (6)$$

354  $a_0 \sim a_6$  and  $b_0 \sim b_3$  are regressed coefficients based on the numerical experiments  
355 under the conditions of urban geometries and atmospheric forcing listed in Table 1 which  
356 can cover most conditions of urban geometric parameters and climate conditions. Thus,  
357 the Eqs. 5 and 6 apply to a broad range of urban and weather conditions.

358 Validation of the relationship between  $T_c$  and  $T_r$ . The high-spatial-resolution airborne  
359 thermal images with 0.5 m spatial resolution were used to extract the component

360 temperatures such as temperatures of wall facets, rooftops, and roads. These images were  
361 observed at 12:40 pm on Aug 5, 2013 and 11:30 am on Oct 24, 2017. The building GIS  
362 data including building shape and height and Digital Surface Model (DSM) data were  
363 used to calculate the  $\lambda_p$  and  $F$  in order to estimate  $T_c$  and  $T_r$  from satellite data, while the  
364 high resolution airborne thermal camera data were applied to determine the component  
365 temperatures for each urban facet. For the high-resolution images, we obtained the mean  
366 component temperatures from different view images. The airborne thermal camera has a  
367 large FOV, so wall information can be acquired from the images. Then,  $T_r$  was estimated  
368 by the nadir high-spatial-resolution airborne thermal images and used to estimate the  $T_c$   
369 based on the relationships constructed as described in this Section 2.5 (Eq.5). The  $T_c$   
370 estimated from component temperatures and  $\lambda_p$  and  $F$  (Eq. 3) was used to validate the  
371 complete surface temperature estimated from  $T_r$  and the relationships described in this  
372 section.

## 373 **2.6 Estimation of $T_c$ from $T_r$**

374 We have demonstrated how the relationship in Eq.5 and Eq.6 can be applied to actual  
375 satellite images. Here we describe briefly the procedure applied, while the results are  
376 presented in Sect.4.4

377 Daytime thermal images acquired by Landsat TM in 2010 were used to retrieve  
378 daytime  $T_r$  and ASTER nighttime thermal images acquired from Mar 13, 2013 and Aug  
379 4, 2013 were used to retrieve  $T_r$  at night. The  $T_c$  images were then estimated by applying  
380 the relationships in Section 2.5 Eqs. (5) and (6).

381 The single channel method for  $T_r$  retrieval was used in this study (Li et al, 2013). For  
382 Landsat TM data, the effective transmittance of the atmosphere in band 6 of Landsat 5,  
383 i.e. the upward and downward atmospheric thermal radiance can be estimated using the  
384 NASA Atmospheric Correction Parameter Calculator (<http://atmcorr.gsfc.nasa.gov/>) to  
385 obtain channel radiance observed at the top of the urban canopy. The band 13 radiance of  
386 ASTER AST 09T product is the ground-leaving in-band radiance including the emission  
387 of surface and the reflected radiance by the surface, and the sky thermal irradiance in  
388 band 13 of the ASTER AST 09T product was used to calculate the downwelling radiance  
389 for the UST retrieval (Sobrino et al, 2007). The radiance leaving urban canopy can be  
390 written as:

$$391 \quad E(i) = \varepsilon(i)B(T_r(i)) + (1 - \varepsilon(i))R_{at}^\downarrow(i) \quad (7)$$

392 In the Equation (7),  $\varepsilon(i)$  is the material emissivity of pixel  $i$ , calculated from the  
393 landcover and building GIS data as Yang et al. (2016) (see Sect. 3.3).  $B(T_r(i))$  is the  
394 upwelling radiance of pixel  $i$  with radiometric temperature  $T_r(i)$ .  $R_{at}^\downarrow(i)$  is the  
395 atmospheric downward radiance. When the effects of topography and geometric  
396 characteristics are considered, the thermal infrared ground-leaving radiance  $E(i)$   
397 comprises the emittance of facets in the observed built-up space, the reflected radiance by  
398 the facets within pixel  $i$  and that by the neighbouring scene elements.

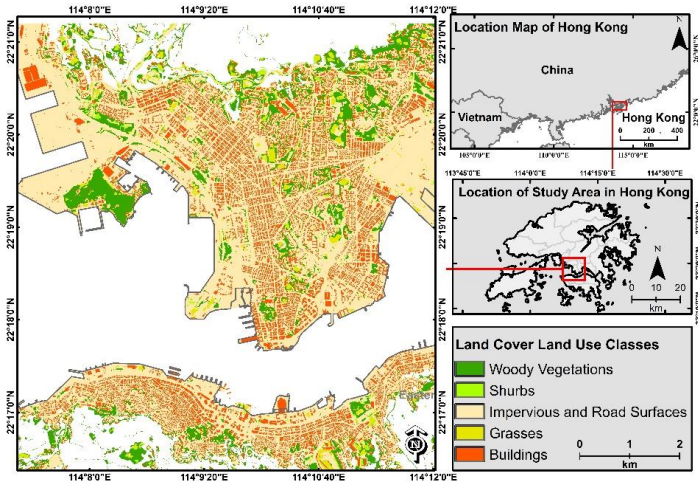
399 The radiometric temperatures were first retrieved with Landsat TM and ASTER data,  
400 then the complete surface temperature was calculated using the retrieved radiometric  
401 temperature (Eqs. 5 and 6). The urban geometric data and land use data were used to  
402 estimate the urban emissivity for the radiometric temperature. The building dataset and

403 Digital Surface Model (DSM) were also used to calculate  $\lambda_p$  and  $F$ . The seasonal effects  
404 on  $T_c$  were analyzed using the Landsat TM and ASTER data.

### 405 **3. Study area and Data**

#### 406 **3.1 Study area**

407 Urban districts of Kowloon peninsula and Hong Kong Island across Hong Kong  
408 were selected as our study area (Figure 1). In brief, Hong Kong is a coastal city in South  
409 China (22° 17' N, 114° 09' E), and this study area has been recognized as a compact city  
410 with high-density living (Chen et al., 2012). Specifically, urban districts of Kowloon  
411 peninsula and Hong Kong Island is highly urbanized with mixed land use and high  
412 population density (Peng et al., 2017). Historical development of these urbanized areas  
413 has also resulted in commercial areas with high-density high-rise built environment for  
414 decades (Peng et al., 2017). Nowadays, there are even two high-rise buildings with more  
415 than 400m across the study area (the International Finance Centre and International  
416 Commerce Centre). Due to this high-rise, high-density urban environment, urban canyons  
417 have formed to influence microclimate significantly (Chen et al., 2012). In this condition,  
418 the remote sensing observation is also limited to part of urban facets. The observed  
419 radiometric surface temperature cannot represent the real urban surface temperature in  
420 such compacted city. Thus, the estimation of  $T_c$  is crucially important for urban climate  
421 research in Hong Kong, as a high quality thermal dataset should enhance the estimation  
422 of microclimate across a compact environment in a three-dimensional context.



423

424 Figure 1. Study area: land uses in Kowloon peninsula and the Hong Kong Island

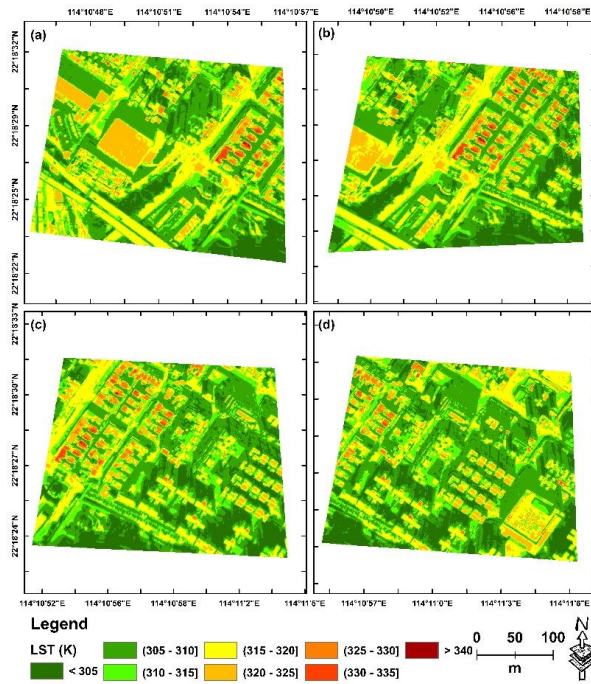
425

426 **3.2 Thermal Remote sensing data**

427 Landsat TM and ASTER data were used to estimate  $T_c$  in Hong Kong. The high  
 428 spatial resolution thermal image data (Figure 2) captured on Aug 5 2013 and Oct 24 2017  
 429 were used in this study for validation. These images are observed at the nadir of the  
 430 central image line. but the FOV of airborne thermal camera is large, so the images  
 431 overlap, i.e. in different images there is the LST of the same target at different view  
 432 angles. The estimated complete surface temperature was validated using the component  
 433 temperatures (wall facets, rooftop and road) captured by the high resolution airborne  
 434 thermal images and building data (Figure 2a to d). Additionally, the building data and  
 435 Digital Surface Model (DSM) data at 1 m spatial resolution were used to calculate  $\lambda_p$  and  
 436  $F$  to estimate the complete surface temperature. More information about building data  
 437 and LiDAR data can be found in Yang et al. (2016). The data acquired by satellite and



438 airborne platforms used in this study are listed in Table 4.



439

440 Figure 2. High spatial resolution thermal images acquired on Aug 5, 2013.

441 Table 4. Overview of satellite and airborne Thermal InfraRed (TIR) images used in this  
 442 study.

Data	Date	Local Time	Resolution(m)	Purpose
Landsat TM Band 6	Jan 14 2010	10:37 am	30 (resampled)	Retrieve $T_r$ and $T_c$
	Mar 26 2010	10:43 am		
	Sept 18 2010	10:42 am		
	Oct 29 2010	10:36 am		
	Nov 11 2010	10:36 am		
	Dec 23 2010	10:42 am		

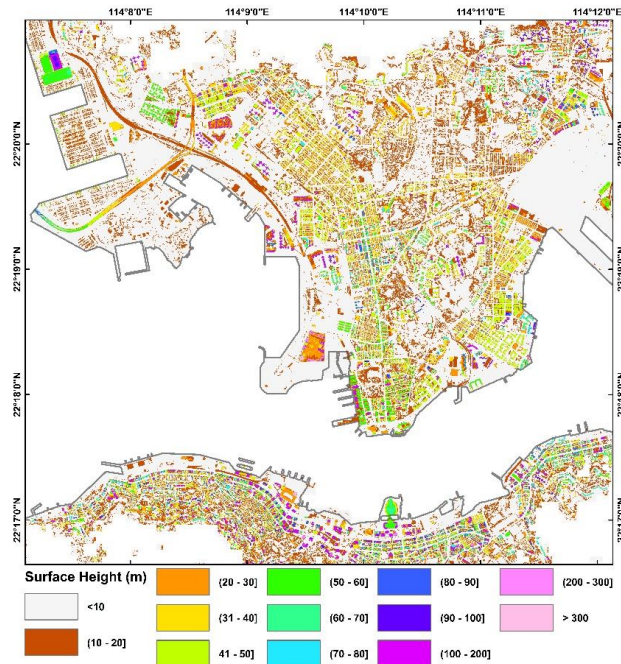
ASTER band 13	Mar 13 2013	10:36 pm	90	
	Aug 4 2013	10:36 pm		
Thermal images from thermal camera (FLIR T650sc) on airborne helicopter (500m)	Aug 5 2013	12:40 pm	0.5	Validation
	Oct 24 2017	11:30 am		

### 443 3.3 Land use and building information

444 We used airborne LiDAR data with 1 m spatial resolution and the building GIS data  
445 provided by the Hong Kong Civil Engineering and Development Department and Hong  
446 Kong Lands Department (Lai et al., 2012) (Figure 1). The LiDAR data were collected in  
447 December 2010 and January 2011 and used to determine and map the building heights  
448 (Figure 3). Land use data provided by the Hong Kong Planning Department and the 2010  
449 building GIS data were used to estimate and map the material emissivity of Hong Kong  
450 (Figure 1). The overall classification accuracy of the land – use data in urban areas was  
451 96% (according to the Hong Kong Planning Department). The land use classification data  
452 provide land cover information, e.g. tree, grassland and impervious surface with a spatial  
453 resolution of 6 m. Building GIS data were used to distinguish the impervious surface in  
454 buildings and road pavements (Figure 1). More information about emissivity estimation  
455 can be referred to Yang et al (2016).

456 The building GIS data and building heights (Figure 3) were used to calculate  $\lambda_p$  and  $F$ .

457 The  $\lambda_p$  with building data was calculated as the ratio of the building roof area to the area  
458 of a pixel, i.e. 30 m x 30 m for Landsat or 90 m x 90 m for ASTER.  $F$  was calculated as  
459 the ratio of the building wall area to the area of a pixel.



460

461 Figure 3. Building heights of Kowloon peninsula and the Hong Kong Island.

### 462 3.4. Ground-level meteorological data

463 The meteorological data used in this study (Table 5) were collected at the weather  
464 station located at the headquarters of the Hong Kong Observatory. Observations used in  
465 the experiments were limited to the time period between 0 am to 24 pm local time of  
466 sunny days in each month of year 2010. These days were selected because of the  
467 cloudless conditions. The air temperature ranges from 5.2 to 32.7 °C. Wind speed ranges  
468 from 0.1 to 4.3 m/s since in Hong Kong there are many high-rise buildings which reduce

469 wind speed in the surface layer. The highest solar irradiance is 1013.89 W/m<sup>2</sup> at noon on  
 470 July 1<sup>st</sup> 2010. These meteorological data can cover most subtropical and mid-latitude  
 471 climate conditions. Extreme cold areas may need further study.

472 Table 5. Overview of the meteorological data used in this study.

Variable	Description (units)	Date	Duration (hourly)
Solar irradiance	W/m <sup>2</sup>	Feb 27 2010, Mar 10 2010,	0~24
Wind speed	m s <sup>-1</sup>	Apr 11 2010, May 25	
Air temperature	°C	2010, Jul 1 2010, Aug 2	
Air pressure at ground surface	mb	2010, Sept 17 2010, Oct 28 2010, Nov 27 2010, Dec 7 2010	

473

#### 474 4. Results

475 The results of the sensitivity analysis described in Sect. 2.3 are presented first (Sect. 4.1),  
 476 followed (Sect. 4.2) by the determination of the simple model described in Sect. 2.4. The  
 477 model is then evaluated against the high resolution TIR image data (Sect.4.3) and applied  
 478 to actual Landsat TM and ASTER image data (Sect. 4.4).

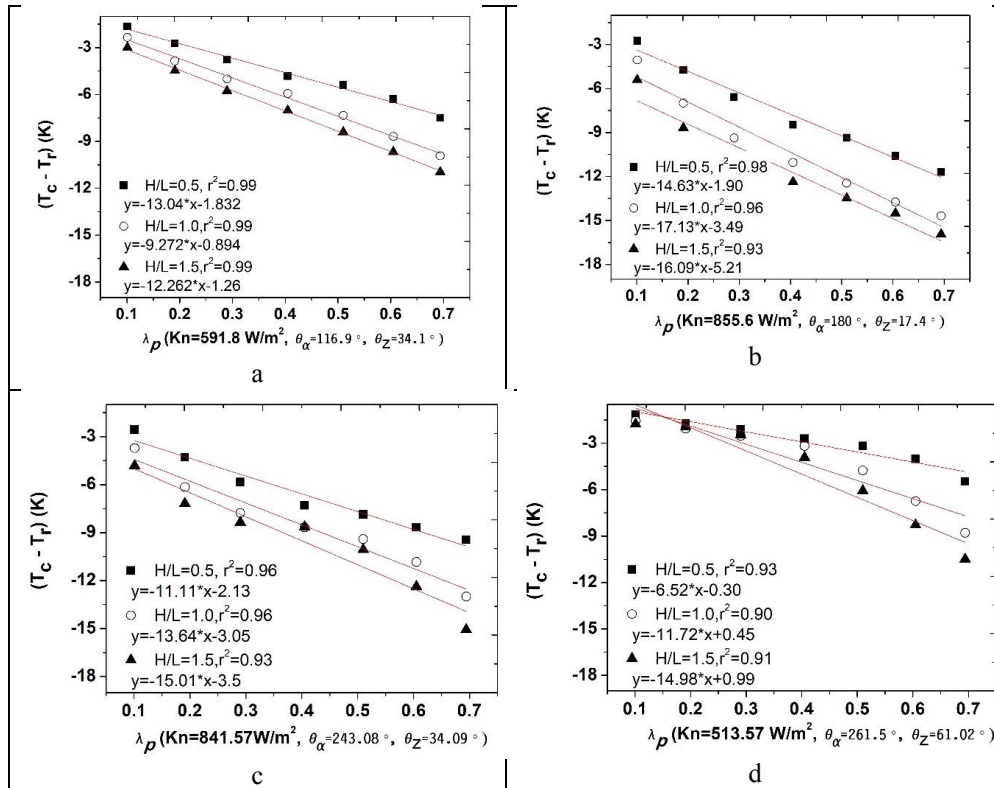
#### 479 4.1 Sensitivity analysis of the relationship between $T_c$ and $T_r$

##### 480 4.1.1 Effects of $\lambda_p$ on difference between $T_c$ and $T_r$

481 A linear relationship between the difference ( $T_c - T_r$ ) and  $\lambda_p$  was found for  
 482 different solar and H/L daytime conditions (Figure 4). In Figure 4, the radiative and

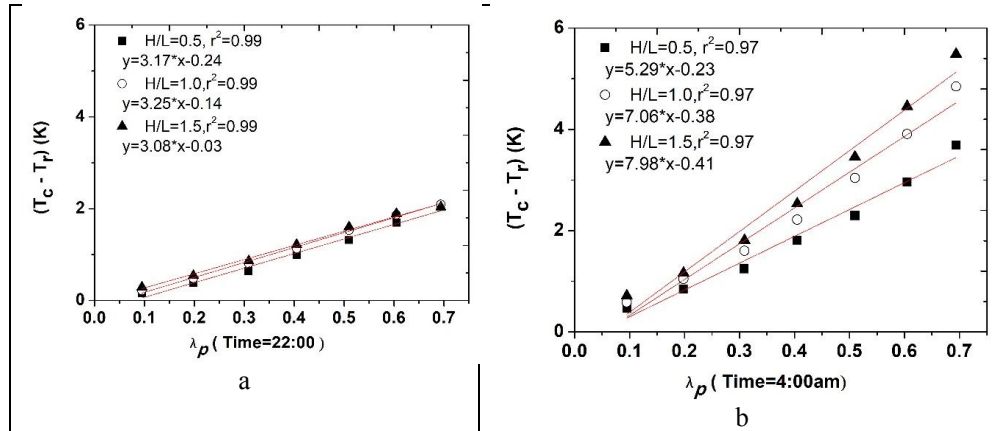
483 thermal properties are set as Group 3 in Table 2. This experiment was performed at  
484 constant values of H/L, wind speed, solar azimuth and zenith angles, i.e. changes in ( $T_c -$   
485  $T_r$ ) were due to changes in  $\lambda_p$  only. Overall,  $T_c - T_r$  increased in magnitude (absolute  
486 difference) with  $\lambda_p$ . With the increase of  $\lambda_p$ , the fraction of irradiance on street/road  
487 facets decreases, while the fraction of irradiance on rooftop facets increases (Yang and Li,  
488 2015). At the same time, the sensible heat flux at wall and street facets decreases with  $\lambda_p$ ,  
489 while the sensible heat flux at roof facets remains nearly constant (Appendix Figure 1a).  
490 The overall sensible heat flux decreases with  $\lambda_p$  due to the skimming effect (Grimmond  
491 and Oke, 1999). During daytime, irradiance on street and wall facets decreases with  
492 increasing  $\lambda_p$  because of the reduced sky view factor. Additionally, the proximity  
493 between street and wall surfaces reduces sky view factors and increases drag on the  
494 airflow reducing the convective heat transfer from the urban canopy to the surface layer  
495 (Nazarian and Kleissl, 2015). The reduced irradiance leads to lower wall surface  
496 temperature and sensible heat flux at wall facets. Note that the dominant factor  
497 influencing canopy surface temperature during daytime is solar radiation. This makes the  
498 wall and street surface temperature to decrease with increasing  $\lambda_p$ . Moreover, the  
499 shading effect makes surface temperature of street and wall facets lower than roof facets.  
500 With the increase of  $\lambda_p$ , a greater portion of the 3D facets cannot be observed by a nadir  
501 viewing imaging radiometer. At the same time,  $T_c$  decreases with increasing  $\lambda_p$  due to the  
502 decrease of wall and street surface temperatures (Appendix Figure 2). The change of  $T_r$   
503 with  $\lambda_p$  is not consistent and depends on the solar zenith angle and building H/L  
504 (Appendix Figure 2) since both the solar angle and building H/L ratio determine  
505 shadows. The difference between  $T_c$  and  $T_r$  changes with local solar time because of the

506 solar position and irradiance. At lower solar zenith angles (Figure 4b), the difference  
 507 between  $T_c$  and  $T_r$  is larger than at higher solar zenith angles (Figure 4d). The linear  
 508 dependence of  $(T_c - T_r)$  on  $\lambda_p$  holds in all cases, but the slope changes with H/L and solar  
 509 position, which should be taken into account in a generalized model. Street orientation  
 510 also affects the irradiance and the shadow distribution and then affects both radiative and  
 511 convective heat transfer. The material properties of roof, street and wall also affect the  
 512 surface temperature distribution. This study did not consider the street orientation and  
 513 material properties, which should be investigated in future work.



514 Figure 4. Relationships between the difference  $(T_c - T_r)$  and  $\lambda_p$  under four different  
 515 daytime solar conditions.

516 In these experiments, the decrease in wall facet temperature at night was generally  
517 smaller than for rooftop temperature. One reason is the attenuation of radiation loss  
518 because of radiative trapping in the urban canyons compared to rapid radiative cooling of  
519 rooftops (Martilli et al., 2002). Overall, the sensible heat fluxes at roof facets and wall  
520 facets are much smaller than in daytime. The sensible heat flux at roof facets is close to  
521 zero and much smaller than the sensible heat flux at wall and street facets (Appendix  
522 Figure 1). This is because the rooftop surface temperature is much lower than the wall  
523 surface temperature at night (Nazarian and Kleissl, 2015). This thus induces a different  
524 urban surface temperature distribution compared with daytime, and this difference is also  
525 captured by the relationship between  $(T_c - T_r)$  and  $\lambda_p$  at night (Figure 5). In addition,  
526 radiative trapping increases with  $\lambda_p$ , thus  $(T_c - T_r)$  at night increases with increasing  $\lambda_p$ .  
527 With increasing  $\lambda_p$ , a larger rooftop fractional area is captured by a nadir viewing  
528 imaging radiometer. The high-density of buildings can reduce the effectiveness of walls  
529 in radiative and convective dissipation of excess energy, which results in higher wall  
530 temperature than rooftops at night (Coutts et al., 2007). These make  $(T_c - T_r)$  at night  
531 increase with increasing  $\lambda_p$ . Higher  $\lambda_p$  implies a smaller sky view factor and results in  
532 higher surface temperature within urban canyons. The cooling rate of wall and ground  
533 facets is much smaller than that of roof facets, thus the temperature of the wall surface is  
534 higher than rooftop, even in the early morning before sunrise (Kusaka and Kimura, 2004;  
535 Nazarian and Kleissl, 2015). This results in nighttime  $T_r$  being lower than  $T_c$ . The  
536 material properties also affect the cooling rate of urban surfaces, as described in a later  
537 section.



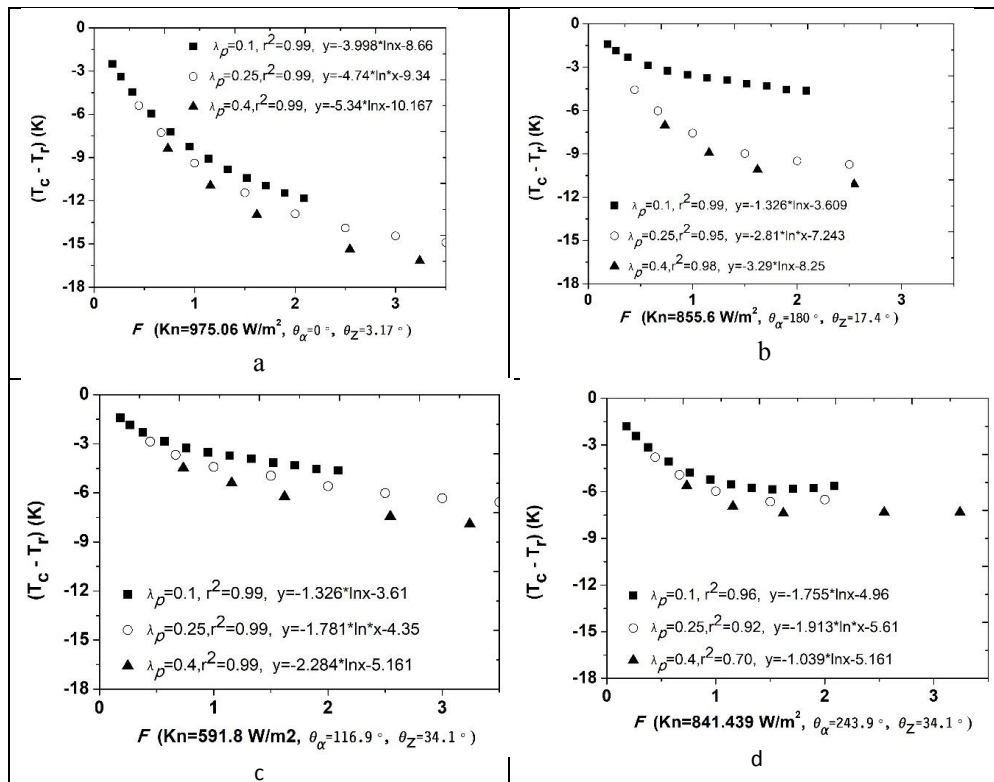
538 Figure 5. Relationship between the nighttime difference  $(T_c - T_r)$  and  $\lambda_p$ .

#### 539 4.1.2 Effects of $F$ on the difference between $T_c$ and $T_r$

540 When  $\lambda_p$  is constant,  $F$  and aspect ratio increase with  $H/L$ . During daytime, the  
 541 relationship between  $(T_c - T_r)$  and  $F$  is logarithmic when aspect ratio is smaller than 3.5  
 542 (Figure 6). When the aspect ratio and  $F$  increase, the street canyon becomes narrower and  
 543 less solar radiation penetrates into the street canyon, thus irradiance onto street and wall  
 544 facets decreases (Ali-Toudert and Mayer, 2006; Lemonsu et al., 2004; Nazarian and  
 545 Kleissl, 2015) Yang and Li, 2015). The increase of aspect ratio contributes to the decrease  
 546 of sensible heat flux at wall and ground facets (Nazarian and Kleissl, 2015). The total  
 547 sensible heat flux increases with increasing aspect ratio, since the frontal area index and  
 548 displacement height increase and, therefore, the aerodynamic resistance decreases. In  
 549 daytime the energy loss by sensible heat exchange is mainly from rooftops (Martilli et al.,  
 550 2002), while the irradiance onto rooftop facets does not vary since the  $\lambda_p$  does not  
 551 change. Overall, these changes lead to a lower rooftop surface temperature. The  
 552 difference between  $T_c$  and  $T_r$  increases gently with increasing  $F$  (Figures 6). The decrease



553 in irradiance is the dominant driver of wall and ground surface temperature, which still  
 554 decreases notwithstanding the decrease in sensible heat flux with  $F$ . When the solar  
 555 zenith angle  $\theta_z$  is larger than 0, the wall and ground surface temperatures decrease less  
 556 than when  $\theta_z$  is equal to 0 (Figure 6d) and  $T_c - T_r$  levels off when  $F$  is higher than a  
 557 threshold  $F^*$ , which depends on irradiance and  $\theta_z$  (Figure 6).

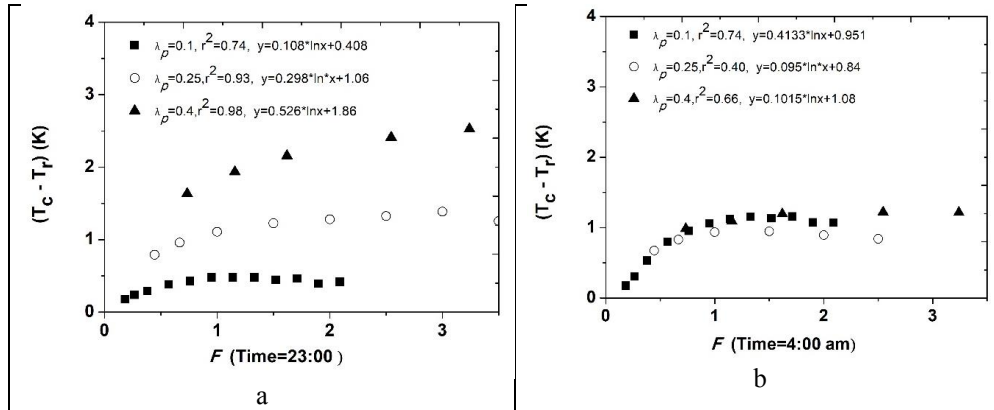


558 Figure 6. Relationship between the daytime difference  $(T_c - T_r)$  and  $F$  under different  
 559 solar conditions.

560 At night,  $T_c - T_r$  increases with  $F$  at constant  $\lambda_p$  and then saturates (Figure 7). A higher  
 561 aspect ratio reduces the sky view factor, longwave emittance and convective heat transfer  
 562 to the atmospheric boundary layer. The sensible heat flux at wall and ground facets

563 decreases with increasing aspect ratio (Nazarian and Kleissl 2015). The cooling rate of  
564 wall and ground facet surfaces at night decreases with increasing aspect ratio, everything  
565 else being the same (Nazarian and Kleissl 2015). Road and wall facets are then cooling  
566 less than rooftop facets and also contributing to a road and wall facet temperature higher  
567 than rooftop facet temperature, resulting in an increase in  $T_c - T_r$  with the aspect ratio.  
568 Convective heat exchange between wall facets and the atmospheric boundary layer  
569 increases with  $F$ , due to the effect of  $F$  on the temperature difference between the urban  
570 canyon and atmospheric boundary layer. This makes the wall surface temperature  
571 decrease, everything else being the same, and  $T_c - T_r$  to level off past an initial increase  
572 with  $F$  (Figure 7). The difference between  $T_c$  and  $T_r$  increases with the 3D complexity of  
573 the observed urban target. It approaches zero with both  $F$  and  $\lambda_p$  approaching zero (i.e.  
574 for a flat target) and it is largest with  $F = 4$  and  $\lambda_p = 0.4$  in Figs. 6 and 7. A higher  $F$ -  
575 value at constant  $\lambda_p$  applies to taller buildings at constant areal (roof) density, while a  
576 higher  $\lambda_p$  at constant  $F$  applies to denser but lower buildings. In both cases an increase in  
577 either  $F$  or  $\lambda_p$  implies that more building facets cannot be observed by a nadir looking  
578 radiometer, thus explaining the increasing difference between  $T_c$  and  $T_r$ .

579

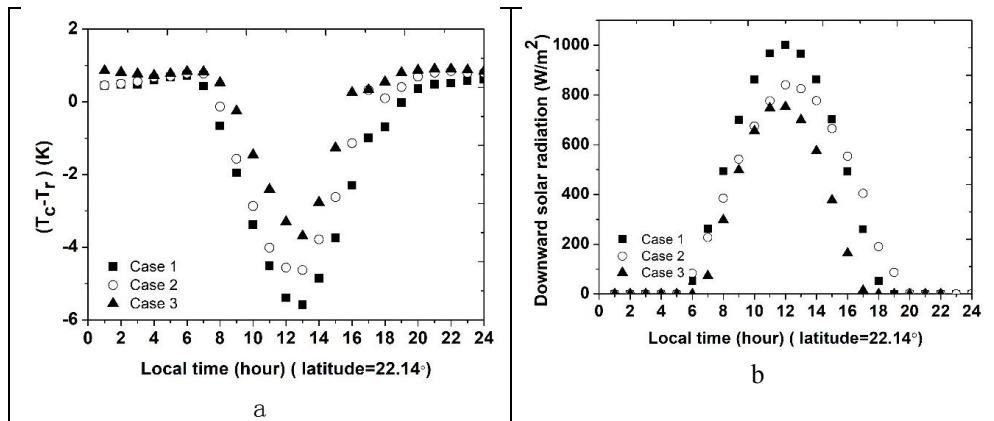


580 Figure 7. Relationship between the nighttime difference  $(T_c - T_r)$  and  $F$ .

### 581 4.1.3 Effects of solar radiation on the difference between $T_c$ and $T_r$

582 The irradiance onto urban surfaces changes with the solar angle, shading pattern and  
 583 shortwave radiation intensity (Nazarian et al., 2017). The surface temperatures of road,  
 584 rooftop and wall facets undergo a very different diurnal thermal cycle due to the solar  
 585 position, urban geometry and material properties (Nazarian and Kleissl, 2015). This  
 586 process contributes to the spatial variability of urban surface temperature and of turbulent  
 587 heat transfer (Nazarian et al., 2018a; Nazarian et al., 2018b). Uneven irradiance caused  
 588 by urban geometry and materials is the main driver of the spatial variability of daytime  
 589 surface temperature under cloudless conditions, which results in the difference between  
 590  $T_c$  and  $T_r$ . The surface temperature of roads and wall facets is lower than roof  
 591 temperature, due to the shadowing effect. The solar zenith angle and azimuth angle vary  
 592 by the hour and day of year, which cast shadows at different locations within the urban  
 593 canopy, thus determining the spatial variability of UST. Additionally, the magnitude of  
 594 surface temperature heterogeneity changes with solar irradiance, e.g. surface temperature  
 595 heterogeneity is higher in summer than in winter in Hong Kong. Figure 8 showed the

596 effects of solar irradiance and solar position on  $(T_c - T_r)$  when  $\lambda_p = 0.25$  and  $H/L = 0.5$ .  
 597 This study used actual observations of solar irradiance on three days (Figure 8b). The  
 598 results showed that when the irradiance is smaller, e.g. case 3 in Figure 8b,  $(T_c - T_r)$  is  
 599 smaller. When the irradiance increases,  $(T_c - T_r)$  increases, since the rooftop temperature  
 600 increases more than the wall temperature (Figure 10b, case 1 and case 2). The higher  
 601 irradiance heats up the rooftop facets, which makes the  $T_r$  observed by remote sensors  
 602 higher than  $T_c$ . The daytime solar radiation has little impact on the nighttime  $T_c - T_r$  3  
 603 hours after sunset, e.g. 9:00 pm (Figure 8a).

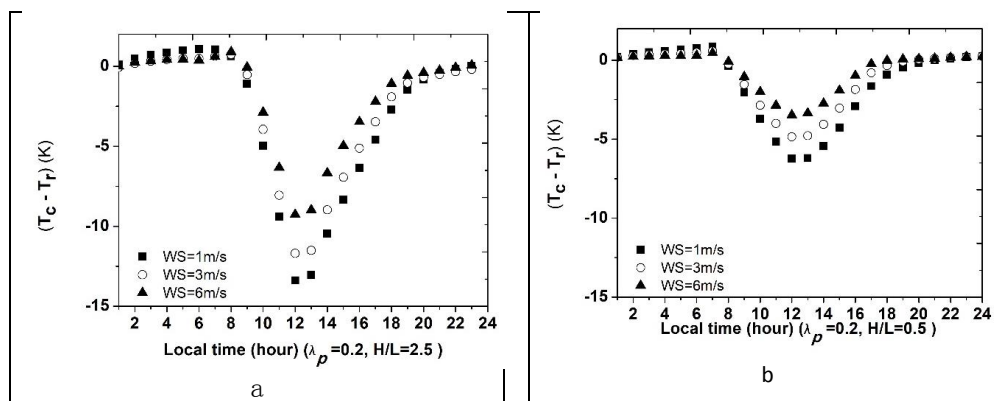


604 Figure 8. Sensitivity of  $T_c - T_r$  to irradiance: a)  $T_c - T_r$  for cases 1 to 3 and; b) irradiance  
 605 cases 1 to 3 as applied in a).

#### 606 4.1.4 Effects of wind speed on the difference between $T_c$ and $T_r$

607 TUF-3D is not originally designed for detailed assessments of the impacts of wind  
 608 speed on surface temperature. This study adopted, however, a first-order evaluation of  
 609 wind speed effects on  $T_c - T_r$ , assuming  $T_r$  to be observed at nadir. In our numerical  
 610 experiments (see Sect. 2.2), wind speed at twice the building height was varied within the

611 range 1 to 6 m s<sup>-1</sup>. The results show that  $T_c - T_r$  decreases with increasing wind speed  
 612 (Figure 9). This effect is particularly strong during daytime for a neighborhood with a  
 613 large wall area, in which case directional shortwave irradiance generates a larger surface  
 614 temperature heterogeneity which is modulated by wind speed. On average, our  
 615 experiments give a sensitivity of  $T_c - T_r$  to wind speed, with a 0.83 K reduction of  $T_c - T_r$   
 616 per 1 m s<sup>-1</sup> increase in wind speed when  $\lambda_p=0.2$  and H/L=2.5. These reductions of  $T_c - T_r$   
 617 with wind speed vary with solar radiation and building density and height (Figure 9).

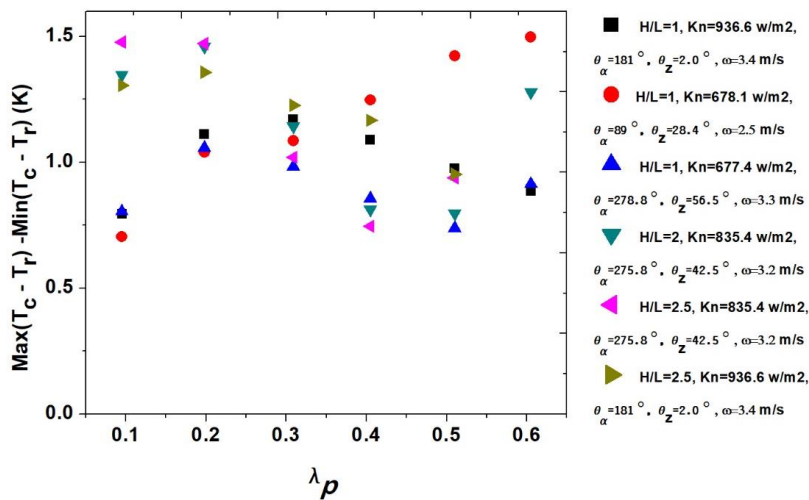


618 Figure 9. Sensitivity of  $T_c - T_r$  to wind speed under different conditions: a,  $\lambda_p=0.2$ ,  
 619 H/L=2.5; b,  $\lambda_p=0.2$ , H/L=0.5.

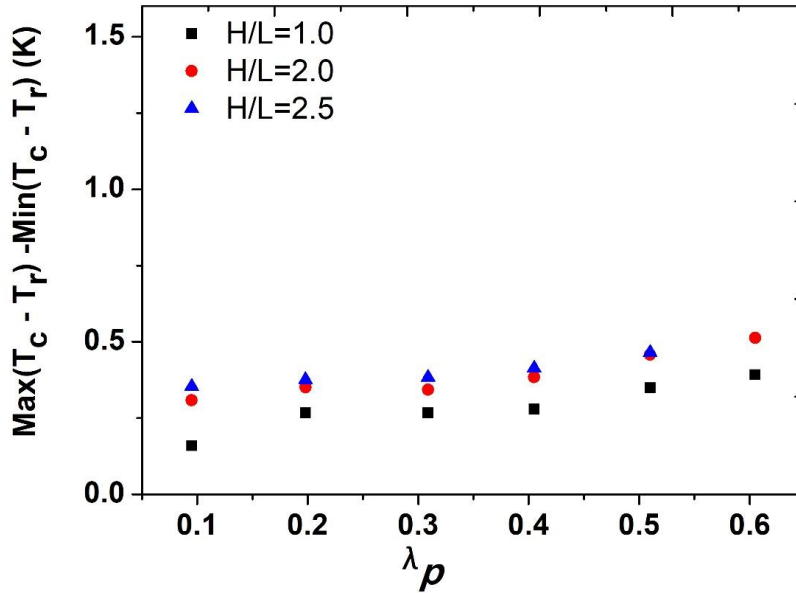
#### 620 4.1.5 Sensitivity of $T_c - T_r$ to material properties

621 The material heterogeneity also causes thermal heterogeneity, but it is difficult to  
 622 obtain exact information on materials in a city. Based on the material properties provided  
 623 by (Stewart et al., 2014), the effects of material properties on  $T_c - T_r$  were studied. Under  
 624 different geometric and meteorological daytime conditions, the different materials can  
 625 cause a 1.5 °C difference in  $T_c - T_r$  (Figure 10). The differences in  $T_c - T_r$  depend on the  
 626 material distribution and solar position, although differences caused by material

627 properties remain much lower than  $T_c - T_r$ . We still recommend however, that the local  
 628 material properties should be used in numerical experiments to study the dependence of  
 629  $T_c - T_r$  on urban conditions. The impact of material properties on  $T_c - T_r$  is smaller during  
 630 nighttime, i.e. less than 0.5 K and increasing with  $\lambda_p$  (Figure 11).



631  
 632 Figure 10. Impact of material properties on daytime  $T_c - T_r$ : ( $\max(T_c - T_r) - \min(T_c - T_r)$ )  
 633 obtained with the TUF – 3D numerical experiments and applying different combinations  
 634 of material properties in Table 2. (the parameter values applying to each experiment are  
 635 listed in the legend: H/L = ratio of building height to length; Kn = solar irradiance;  $\theta_a$  =  
 636 sun azimuth angle;  $\theta_z$  = sun zenith angle;  $\omega$  = wind speed)



637

638 Figure 11. Impact of material properties on nighttime  $T_c - T_r$  : ( $\max(T_c - T_r) - \min(T_c - T_r)$ )  
 639 obtained with the TUF – 3D numerical experiments and applying different combinations  
 640 of material properties in Table 2. (the parameter values applying to each experiment are  
 641 listed in the legend: H/L = ratio of building height to length)

#### 642 4.2 Development of a simple empirical model to estimate $T_c - T_r$

643 The dependence of  $T_c - T_r$  on geometric and climate variables and parameters has  
 644 been explored in Sect 4.1. This analysis suggests that  $T_c - T_r$  depends linearly on  $\lambda_p$  and  
 645 the solar parameters ( $\text{Kn}$ ,  $\theta_a$ ,  $\theta_z$ ), while the dependence on  $F$  is logarithmic.

646 Building upon these findings, a simple empirical model (see Eq. 5 ) to estimate  $T_c$   
 647 from  $T_r$ .  $f_d$  was constructed for daytime conditions by fitting Eq. 5 to the pseudo –  
 648 observations generated by numerical experiments (Table 6). Two options were explored:  
 649 a) by binning the pseudo – observations according to wind speed in steps of  $1 \text{ ms}^{-1}$  (see

650 first four cases in Table 6); b) by pooling the pseudo – observations for the entire range in  
 651 wind – speed (Eq. 8). The RMSE increases with the wind speed (Table 6), but the RMSE  
 652 for case (b) is still acceptable and not much larger than in three out of four (a) – cases,  
 653 with  $r^2 = 0.97$  for case (b). We can then conclude that a simple empirical model applies to  
 654 a broad range of geometry and climate conditions and that it is not strictly needed to  
 655 include wind–speed as a predictive variable. This is the empirical model we evaluated  
 656 against high resolution airborne TIR images (Sect.4.3) and applied to satellite TIR  
 657 (Sect.4.4).

658 Larger RMSEs were found when fitting the same model to pseudo – observations  
 659 applying to sunrise (8 am) and sunset (5 pm), due to heat convection rather than solar  
 660 irradiance being the main driver of UST at this time of the day (moreover with  $T_c - T_r$   
 661 being rather small). In contrast, the spatial variability in UST around noon, i.e. from  
 662 11am to 3pm is driven by uneven irradiance associated with urban geometry.  
 663 Accordingly, a smaller bias for estimated  $T_c$ , i.e.  $\text{RMSE} < 1 \text{ K}$ , was achieved by  
 664 combining meteorological and urban geometry parameters. The numerical experiments  
 665 suggest that the inclusion of urban geometry parameters is most significant in modelling  
 666  $T_c$  in the afternoon.

667 Table 6 Estimation of daytime  $T_c$  from  $T_r$ : regression relationships for different  
 668 ranges in wind speed.

Wind speed (m/s)	Regression model	$r^2$	RMSE (K)
------------------	------------------	-------	----------



0~1	$T_c=1.065*T_r-2.883*\lambda_p -0.093*\ln(F) -$ $0.021*Kn+0.014*\theta_a-0.088*\theta_z-10.509$	0.94	0.70
1~2	$T_c=0.930*T_r-6.757*\lambda_p -0.856*\ln(F) -0.006*Kn-$ $0.003*\theta_a+0.053*\theta_z+20.003$	0.97	1.15
2~3	$T_c=0.927*T_r-6.509*\lambda_p -1.023*\ln(F) +0.003*Kn-$ $0.020*\theta_a+0.181*\theta_z + 14.384$	0.97	1.31
3~4	$T_c=0.773*T_r-3.712*\lambda_p -1.730*\ln(F) +0.004*Kn-$ $0.001*\theta_a+0.139*\theta_z + 59.377$	0.96	1.58

669

670 When the wind speed ranges from 0 to 6 m/s, the relationship to estimate  $T_c$  from  $T_r$   
671 at daytime can be written as:

$$672 T_c =0.913*T_r-5.390*\lambda_p -1.090*\ln(F) +0.001*Kn-0.013*\theta_a+0.139*\theta_z+20.598 \quad (8)$$

673 Which gives  $r^2=0.97$ , RMSE=1.500 K . The plot of  $T_c$  simulated by TUF-3D and  
674 estimated by Eq. 8 is presented in Figure 12a.

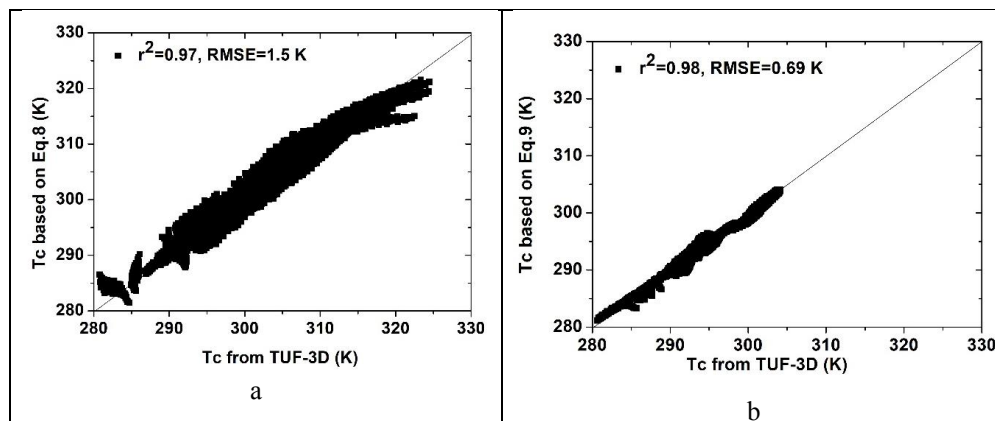
675 During nighttime,  $T_c-T_r$  levels off and it is rather small from 9 pm to 6 am (Figure 8),  
676 while wind speed has a limited effect (Figure 9). Urban geometry still affects the energy  
677 exchange and yields uneven cooling during nighttime, thus leading to the predictive  
678 parameters to include in our simple empirical model (see Eq.6). Finally, the relationship  
679 to estimate  $T_c$  from  $T_r$  at nighttime can be written as:

$$680 T_c=0.927*T_r+3.455*\lambda_p+0.184*\ln(F)+21.320 \quad (9)$$

681 Which gives  $r^2=0.98$ , RMSE=0.690 K. The plot of  $T_c$  simulated by TUF-3D and  
682 estimated by Eq. 9 is presented in Figure 12b.

683 When  $F$  is close to 0 and the surface is flat,  $T_c$  tends to  $T_r$ . The developed  
684 logarithmic function (see Eq. 8 and 9) would give undefined values in the limiting case  $F$   
685  $= 0$ . Even very small values of  $F$ , e.g.  $F = 0.001$  and  $\lambda_p = 0.1$ , however, give a realistic  
686 value of 0.045 K for  $T_c - T_r$  when applying Eq. 9 to a nearly flat surface with 280 K. To  
687 avoid any ambiguity, therefore, a threshold should be defined, e.g.  $F > 0.001$ , to constrain  
688 the range of validity of Eq. 8 and Eq. 9.

689 This empirical model was applied to estimate  $T_c$  from  $T_r$  retrieved from the ASTER  
690 nighttime data (see Sect.4.4).



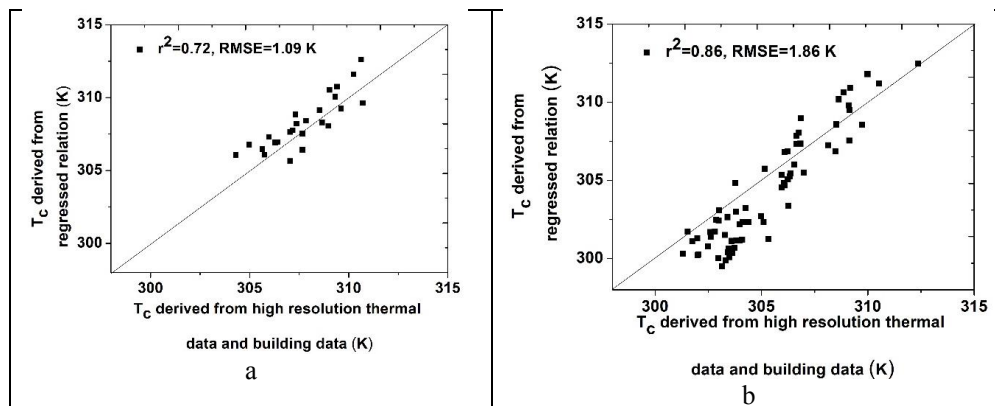
691 Figure 12. Scatter plot between actual and estimated  $T_c$  in the process of determining  
692 the coefficients: a,  $T_c$  from Eq. 8; b,  $T_c$  from Eq. 9.

### 693 4.3 Evaluation with high resolution airborne thermal data

694 Two experiments were conducted to evaluate our simple empirical model using high  
695 spatial resolution thermal infrared image data acquired on Oct 24, 2017 and Aug 5, 2013,  
696 where Oct 24, 2017 represents a day with lower solar irradiance ( $700 \text{ W/m}^2$ ) and Aug 5,  
697 2013 was a day with higher irradiance ( $878.2 \text{ W/m}^2$ ). In addition, wind speed was rather

698 low and similar, i.e. 2 - 3 m s<sup>-1</sup> on both dates, so that we expected a larger thermal  
699 heterogeneity.

700 According to the methodology described above, we calculated the component  
701 temperatures within each 30 m x 30 m grid by averaging the 0.5 m x 0.5 m surface  
702 temperature for each surface type. Then we obtained the  $T_c$  from these component  
703 temperatures by Eq. 3. Then we estimated  $T_c$  from  $T_r$  by applying our Eq. 8 and evaluated  
704 our estimates against the  $T_c$  values obtained from the high resolution thermal images. We  
705 then compared these two sets of  $T_c$  (Figures 13a and 13b). We used the urban geometric  
706 parameters in our empirical relationships and the component temperatures derived from  
707 high-resolution images (Figure 2) at different view angles to determine the wall facet  
708 temperatures and the reference  $T_c$ . This validation gave reasonably accurate estimates of  
709  $T_c$ , consistent with the expected accuracy of our empirical model (Eq. 8), with  $r^2 = 0.75$   
710 and RMSE = 1.09K on Aug 5, 2013 and  $r^2 = 0.86$  and RMSE = 1.86K on Oct 24, 2017  
711 (Figure 13b).



712 Figure 13. Comparison between  $T_c$  derived from  $T_r$  and  $T_c$  retrieved from component  
713 temperatures based on high resolution airborne thermal images: a, on Aug 5, 2013; b, Oct

714

24, 2017.

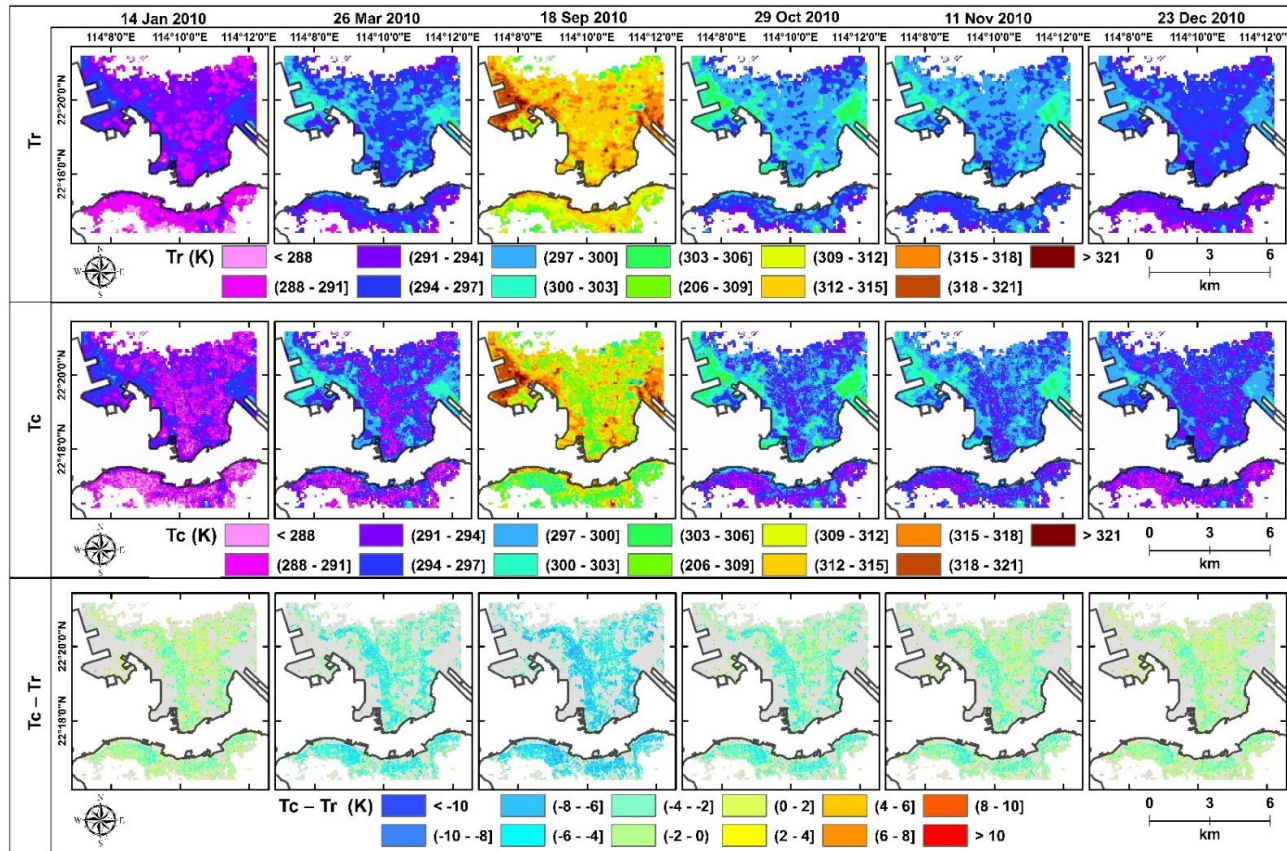
#### 715 **4.4 Complete urban surface temperature from satellite data**

716 Finally, we estimated the daytime and nighttime complete urban surface temperature  
717 by applying our empirical models to Landsat TM and ASTER TIR image data  
718 respectively (Figures 14 and 15).

719 The previous sections and findings suggested that the procedure (Eq. 8) can be applied  
720 to an entire Landsat TM Band 6 image. The results showed that  $T_c$  over built-up areas  
721 was lower than over impervious areas and that during daytime,  $T_r$  was generally higher  
722 than  $T_c$ . The mean value of  $(T_c - T_r)$  was -2.15 K while in extreme cases it reached -6 K  
723 in built-up areas on Dec 23, 2010.  $T_c - T_r$  has a strong seasonal trend associated with urban  
724 morphology and solar position (Table 7). For example, the mean value of  $T_c - T_r$  on Sept  
725 18, 2018, 2010 was -4.98K with extreme values as low as -10 K across built-up areas.  
726 This was possibly due to solar irradiance being the main driver of spatial variability of  
727 UST in daytime during the summer, when  $T_r$  is much higher than  $T_c$ , also taking into  
728 account the impact of shadows in the urban canyon, as determined by solar position. On  
729 the other hand, the solar elevation on Sept 18 2010 was much higher than on the other  
730 days (14 Jan 2010, 26 Mar 2010, Oct 29 2010, Nov 11 2010, Dec 23 2010), which  
731 determined the extreme  $(T_c - T_r)$  values. The higher solar elevation leads to rooftop  
732 temperatures higher than wall facet temperatures, since solar irradiance on the wall facets  
733 is lower. This result is also demonstrated by an increase in  $(T_c - T_r)$  when the solar  
734 elevation decreases and solar irradiance on the wall facets increases.

735  $T_c$  was higher than  $T_r$  in several built-up areas during spring, autumn and winter,

736 while  $T_c$  was lower than  $T_r$  in almost all urban areas during summer. The mean absolute  
737 value of  $(T_c - T_r)$  was nearly equal to the absolute value of mean  $(T_c - T_r)$  on Sept 8, 2010,  
738 while the absolute value of mean  $(T_c - T_r)$  on the other dates was much lower than the  
739 mean absolute value (Table 7). This is possibly due to a lower  $T_r$  across several built-up  
740 areas in non-summer seasons because of lower solar elevation angle, especially in the  
741 areas with fewer high-rise buildings and lower density.



742

743 Figure 14. Radiometric,  $T_r$ , complete,  $T_c$ , surface temperature and their difference  $T_c - T_r$ , retrieved from Landsat TM Band 6 in 2010

744 based

on

Eq.8.

745 Table 7. Difference of  $T_c - T_r$  between complete and radiometric urban surface  
 746 temperature in entire images.

<b>Date</b>	<b>Mean (<math>T_c - T_r</math>) (K)</b>	<b>Mean absolute value of (<math>T_c - T_r</math>) (K)</b>
Jan 14 2010	-0.861	2.133
Mar 26 2010	-3.233	3.640
Sept 18 2010	-4.981	5.133
Oct 29 2010	-2.442	3.00
Nov 30 2010	-1.720	2.530
Dec 23 2010	-0.910	2.150
Mar 13 2013	0.310	0.784
Aug 4 2013	-0.230	0.680

747

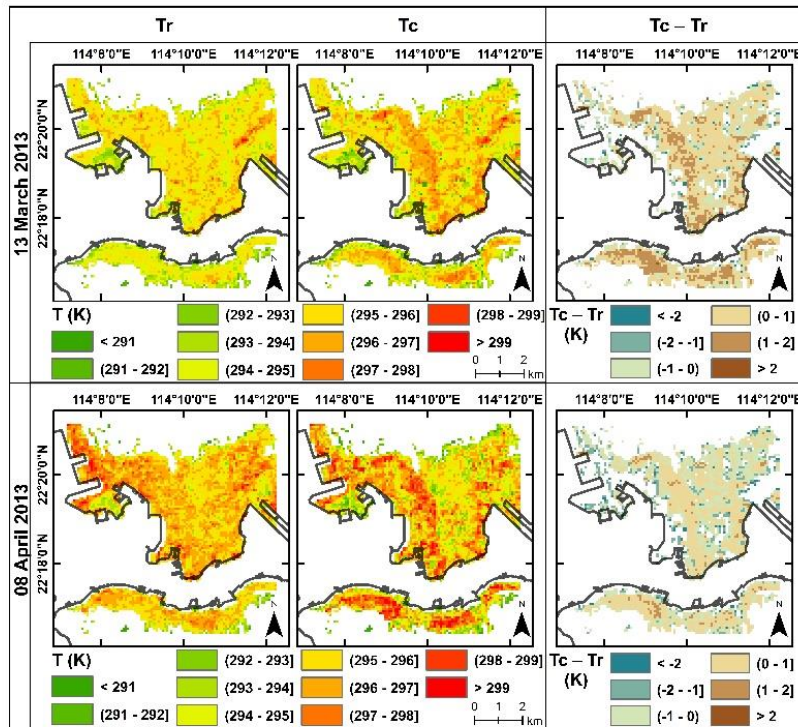
748 The nighttime  $T_c$  was estimated by applying Eq. (9) with ASTER-TIR radiometric  
 749 data and building data. The  $T_c$  was found to be higher than  $T_r$  over built-up areas,  
 750 with the difference reaching 2 K (Figure 14). The Nighttime ( $T_c - T_r$ ) was higher in  
 751 spring than in summer, while the daytime ( $T_c - T_r$ ) was lower in summer than in  
 752 winter. Average and standard deviation of ( $T_c - T_r$ ) during the summer nighttime (Aug  
 753 4, 2013) were -0.21K and 1.13K respectively, while average and standard deviation  
 754 on a winter nighttime (Mar 13 2013) were 0.30 K and 1.13 K respectively.

755 Specifically, in a high-density built environment,  $T_c$  was higher than  $T_r$  at night of  
 756 both Mar 13 and Aug 4 2013. Lower nighttime  $T_r$  then  $T_c$  can be explained by heat  
 757 dissipation at rooftop facets being larger than at wall or street facets. This process of  
 758 radiative and convective dissipation is different in daytime, which may result in a

759 lower rooftop surface temperature in the late evening. The latter is likely to determine  
760 the  $T_r$  observed by a nadir looking TIR imaging radiometer.

761 Another important factor is daytime heat storage and nighttime heat dissipation by  
762 wall facets. The solar elevation angle on Mar 13, 2013 was lower than on August 4  
763 2013, thus solar irradiance on wall facets was higher in August, and it induced  
764 increasing heat storage at wall facets. In addition, building morphology can reduce  
765 both radiative and convective cooling of wall facets: wall facet temperature can be  
766 higher than rooftop temperature at night. Solar irradiance on wall facets is lower in  
767 summer daytime and rooftop temperature decreases rapidly after sunset. This  
768 increases the spatial variability of surface temperature during summer daytime, but  
769 reduces it during summer nighttime. Thus, the spatial variability of surface  
770 temperature at night in summer is smaller than in spring.  $T_c$  on August 4 2013 was  
771 lower than  $T_r$  in areas with lower building density. This is because the wall facet  
772 temperature is lower than the rooftop temperature in some areas at night. In winter,  
773 the solar radiation heats up more wall facets within the urban space because of the  
774 lower solar elevation angle than in summer. Thus, the wall facet temperature in  
775 winter is higher than rooftop temperature, while the wall facet temperature in summer  
776 is a little higher than the rooftop temperature.





777

778 Figure 15. Nighttime  $T_r$  and  $T_c$  estimated by applying Eq.9 from ASTER image data  
 779 and GIS building data in 2013.

780 **5. Discussion**

781 In this study, the TUF-3D model was used to derive synthetic data on urban climate  
 782 under different and controlled conditions. The data from TUF-3D model were used to  
 783 analyze the effects of different urban geometric and climate parameters on the  
 784 relationship between  $T_c$  and  $T_r$  in daytime and nighttime. In addition, the numerical  
 785 experiments showed that the geometric effects on the relationship between  $T_c$  and  $T_r$  are  
 786 different at daytime and nighttime. It is difficult to obtain this information based on

787 observational data. This study demonstrates an operational method to estimate  $T_c$  from  
788 satellite TIR data. The method developed in this study has been validated using the  
789 thermal infrared image data at high spatial resolution. In principle, it would be ideal to  
790 acquire the high resolution TIR image data simultaneously with either the Landsat TM or  
791 ASTER acquisitions for evaluating the estimated  $T_c$ , but this was not feasible due to  
792 practical constraints on the airborne acquisitions. The accuracy of the retrieval of  $T_r$  with  
793 Landsat TM and ASTER radiometric data is well documented in the literature (Li et al.,  
794 2013; Gillespie et al., 1998).

Formatted: Underline, Highlight

795 This study only discussed the estimation of  $T_c$  from nadir viewed remote sensing  
796 thermal data. (Jiang et al., 2018) estimated  $T_c$  from airborne thermal data at different  
797 view angles and results showed that the observed radiometric temperature is closest to  $T_c$   
798 when viewing azimuth and zenith angles are  $\theta_a \pm 90^\circ$  and  $\theta_z = 45 \sim 60^\circ$ . For off-nadir  
799 images, the data can capture information on wall facets, and results show that the  
800 observed  $T_r$  at off-nadir angles is closer to  $T_c$  than the nadir data. (Jiang et al., 2018) also  
801 indicated that  $T_c$  can be improved by measuring directional radiometric temperatures.  
802 Currently the SENTINEL-3 SLSTR can provide two-angular thermal images at nadir and  
803 forward direction (about  $53^\circ$ ), extending the data record collected by the (A)ATSR series  
804 instruments ([https://sentinel.esa.int/web/sentinel/technical-guides/sentinel-3-  
805 slstr/instrument](https://sentinel.esa.int/web/sentinel/technical-guides/sentinel-3-slstr/instrument)). This may provide an opportunity to estimate the complete surface  
806 temperature in the future, albeit at low spatial resolution.

807 It is difficult to obtain the exact material properties within the mixed pixels. Several  
808 studies have shown that geometry is the main determinant of the urban surface

809 temperature distribution (Krayenhoff and Voogt, 2016; Voogt and Oke, 2003), while the  
810 material properties still have impact on urban surface temperature distribution. In  
811 alternative, this study used the predefined material properties of urban surface models to  
812 better evaluate the relationships between  $T_c$  and  $T_r$  associated with urban materials. This  
813 approach may reduce the bias caused by material heterogeneity, while exact information  
814 on material properties within a pixel cannot be obtained from satellite images. Sensitivity  
815 tests also have been conducted using different typical material properties provided by  
816 (Stewart et al., 2014), and results showed that the different material properties caused less  
817 than 1.5 °C spread under different geometric and meteorological conditions. This proved  
818 that urban geometry has more effect on urban surface temperature distribution than  
819 materials. However, we still recommend that the local material properties should be used  
820 in further studies.

821 The TUF-3D can model the radiation and energy flux applying to simple building  
822 arrays. Therefore, the complexity of building shape and distributions in real-world, and  
823 its associated effects on surface temperature distribution have not been explored. The  
824 validation was also carried out over areas without vegetation. In addition, the actual  
825 building outlines and structures are not as uniform as in the TUF-3D model. Thus, the  
826 simple model developed in this study to estimate the complete urban surface temperature  
827 still needs more detailed validation e.g. with in-situ measurements with radiometers or  
828 IR-temperature sensor. The solar irradiance and position at a particular location vary  
829 across seasons. In this study, the latitude was set as 22.14°N. The relationships between  
830  $T_r$  and  $T_c$  at different latitudes will be studied further.

831 We only considered the UST heterogeneity caused by buildings within a pixel, while

832 buildings in neighboring pixels may also influence the spatial variability of temperature  
833 by shadowing effect and interference on heat convection. In this study, the highest  
834 building is 415.8 m. The shadow of this building may affect adjacent pixels, especially at  
835 sunrise and sunset. Thus, our empirical models are more suitable for a city with lower  
836 fractional abundance of high-rise buildings.

837 In this study, the impacts of vegetation cover on temperature was excluded since  
838 Hong Kong is an extremely urbanized area. However, vegetation may have a strong  
839 effect in some cities with complex interactions, due to the shape and density of vegetation  
840 canopy and building morphology. In addition, evapotranspiration of vegetation cover can  
841 significantly reduce urban temperatures. Vegetation cover reduces the wind speed and sky  
842 view factor. Therefore, further applications using the empirical models developed in this  
843 study to other cities may need to require refinements by including the effects of  
844 vegetation.

845 Finally, wind direction was not included in the modelling. Although wind direction is  
846 important in urban energy exchange, it is mostly influencing areas with regular  
847 orientation of streets and identical city blocks. However, considering that orientation of  
848 streets is not regular across Hong Kong (Nichol and Wong, 2005), wind direction may  
849 not have a strong effect on UST. For future studies in a city with regularly oriented  
850 streets, integration with the relative angle between wind and street orientation may be  
851 essential.

## 852 **6. Conclusion**

853 This study explored the relationship between complete urban surface temperature and

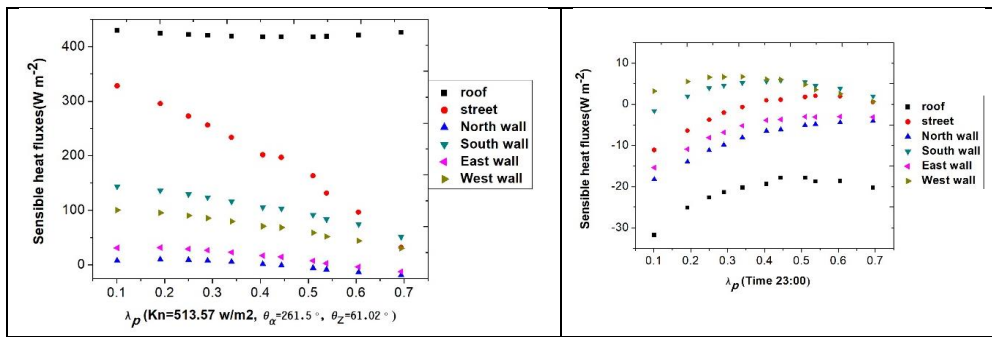
854 the nadir radiometric temperature observed from satellites. The relationships between  
855 urban geometry and difference between  $T_r$  and  $T_c$  were developed and results showed that  
856 the correlation coefficients are 0.97 for daytime and 0.98 for nighttime, and overall  
857 RMSEs are 1.5°C for daytime and 0.69°C for nighttime. Daytime relationships between  $T_r$   
858 and  $T_c$  have been evaluated in this study using higher resolution airborne thermal images  
859 and results showed that the correlation coefficients and RMSEs are 0.72, 1.09°C on  
860 August 6, 2013 at 12:40 pm; and 0.86 and 1.86°C on October 24, 2017 at 11:30 am. The  
861 developed relationships were also used to estimate the complete surface temperature from  
862 satellite data in Hong Kong. The results showed that daytime difference between  $T_c$  and  
863  $T_r$  can reach 10°C in summer and 6°C in winter, and the difference at night can reach to  
864 2°C in spring and summer. This study provides a simplified method for estimating  
865 complete surface temperature from satellite data, and the multi-angular TIR radiometric  
866 data will be used to improve the estimation of urban complete surface temperature in the  
867 near future.

#### 868 **Acknowledgement**

869 This work was supported in part by the grant of Early Career Scheme (project id:  
870 25201614) from the Research Grants Council of Hong Kong, the grant 1-ZE24 from the  
871 Hong Kong Polytechnic University; and Grants by National Natural Science Foundation  
872 of China (41671430, 41901283, 41571366, 61976234, 61601522) and grant number 69-  
873 18ZX10347 by Guangzhou University. The authors thank the Hong Kong Planning  
874 Department, Hong Kong Lands Department, the Hong Kong Civil Engineering and  
875 Development Department, the Hong Kong Observatory and the Hong Kong Government  
876 Flying Service for the planning, building GIS, weather and climate, and airborne Lidar

877 data, and NASA LP DAAC for the Landsat and ASTER satellite imagery. Massimo  
 878 Menenti acknowledges the support of grant P10-TIC-6114 by the Junta de Andalucía and  
 879 the SAFEA Long-Term-Projects of the 1000 Talent Plan for High-Level Foreign Experts  
 880 (grant No. WQ20141100224).

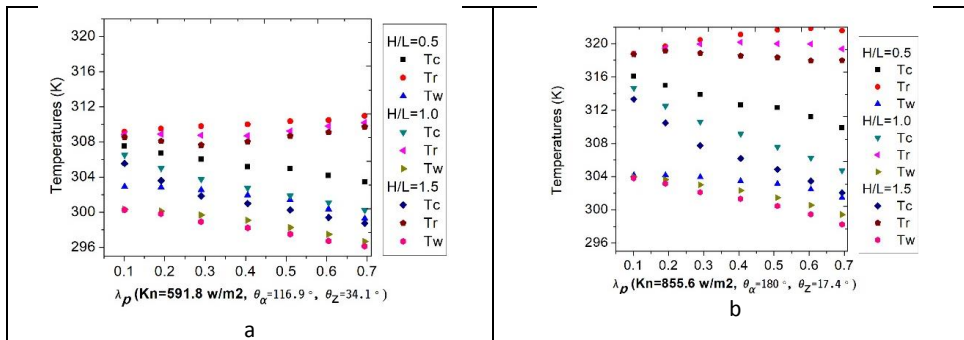
881 **Appendix**

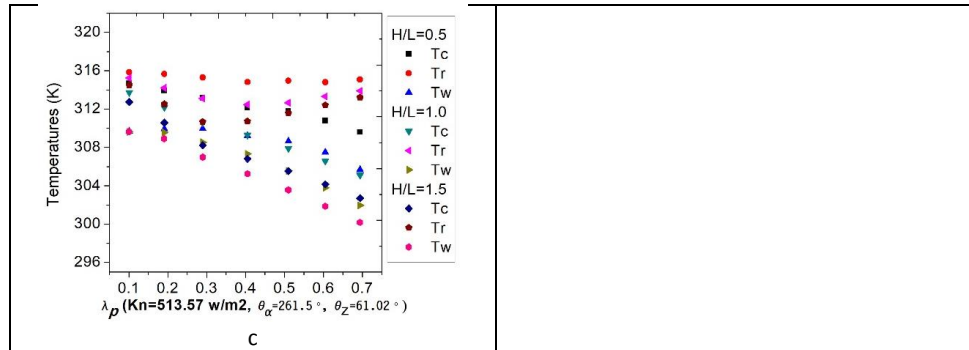


882

883 Figure 1 Change of sensible heat fluxes with  $\lambda_p$ : a daytime; b nighttime.

884





885

886 Figure 2. Change of  $T_r$  and  $T_c$  and  $T_w$  (wall surface temperature) with  $\lambda_p$ .

887

888

889 **References:**

890 Adderley, C., Christen, A. and Voogt, J.A., 2015. The effect of radiometer placement and  
891 view on inferred directional and hemispheric radiometric temperatures of an  
892 urban canopy. *Atmos. Meas. Tech.*, 8(7): 2699-2714.

893 Ali-Toudert, F. and Mayer, H., 2006. Numerical study on the effects of aspect ratio and  
894 orientation of an urban street canyon on outdoor thermal comfort in hot and dry  
895 climate. *Building and Environment*, 41(2): 94-108.

896 Allen, M., Voogt, J. and Christen, A., 2018. Time-Continuous Hemispherical Urban  
897 Surface Temperatures. *Remote Sensing*, 10(1): 3.

898 Arnfield, A.J., 2003. Two decades of urban climate research: a review of turbulence,  
899 exchanges of energy and water, and the urban heat island. *International Journal of  
900 Climatology*, 23(1): 1-26.

901 Arnfield, A.J. and Grimmond, C., 1998. An urban canyon energy budget model and its  
902 application to urban storage heat flux modeling. *Energy and buildings*, 27(1): 61-  
903 68.

904 Becker, F. and Li, Z.L., 1995. Surface temperature and emissivity at various scales:  
905 Definition, measurement and related problems. *Remote Sensing Reviews*, 12(3-4):  
906 225-253.

907 Chen, L. et al., 2012. Sky view factor analysis of street canyons and its implications for  
908 daytime intra- urban air temperature differentials in high- rise, high- density  
909 urban areas of Hong Kong: a GIS- based simulation approach. *International  
910 Journal of Climatology*, 32(1): 121-136.

911 Cheng, J., Liang, S., Wang, J. and Li, X., 2010. A Stepwise Refining Algorithm of  
912 Temperature and Emissivity Separation for Hyperspectral Thermal Infrared Data.  
913 *IEEE Transactions on Geoscience and Remote Sensing*, 48(3): 1588-1597.

914 Coutts, A.M., Beringer, J. and Tapper, N.J., 2007. Impact of Increasing Urban Density on  
915 Local Climate: Spatial and Temporal Variations in the Surface Energy Balance in

916 Melbourne, Australia. *Journal of Applied Meteorology and Climatology*, 46(4):  
917 477-493.

918 Dousset, B. and Gourmelon, F., 2003. Satellite multi-sensor data analysis of urban  
919 surface temperatures and landcover. *ISPRS Journal of Photogrammetry and*  
920 *Remote Sensing*, 58(1-2): 43-54.

921 Grimmond, C. et al., 2011. Initial results from Phase 2 of the international urban energy  
922 balance model comparison. *International journal of climatology*, 31(2): 244-272.

923 Grimmond, C. et al., 2010. The international urban energy balance models comparison  
924 project: first results from phase 1. *Journal of applied meteorology and climatology*,  
925 49(6): 1268-1292.

926 Grimmond, C. and Oke, T.R., 1999. Aerodynamic properties of urban areas derived from  
927 analysis of surface form. *Journal of Applied Meteorology*, 38(9): 1262-1292.

928 Gillespie, A. et al., 1998. A temperature and emissivity separation algorithm for  
929 Advanced Spaceborne Thermal Emission and Reflection Radiometer (ASTER)  
930 images. *Geoscience and Remote Sensing, IEEE Transactions on*, 36(4): 1113-  
931 1126.

932 Jiang, L. et al., 2018. Remote estimation of complete urban surface temperature using  
933 only directional radiometric temperatures. *Building and Environment*, 135: 224-  
934 236.

935 Kanda, M., Kanega, M., Kawai, T., Moriwaki, R. and Sugawara, H., 2007. Roughness  
936 Lengths for Momentum and Heat Derived from Outdoor Urban Scale Models.  
937 *Journal of Applied Meteorology and Climatology*, 46(7): 1067-1079.

938 Kanda, M. et al., 2005. A simple energy balance model for regular building arrays.  
939 *Boundary-Layer Meteorology*, 116(3): 423-443.

940 Kastendeuch, P.P. and Najjar, G., 2009. Simulation and validation of radiative transfers  
941 in urbanised areas. *Solar Energy*, 83(3): 333-341.

942 Kastendeuch, P.P., Najjar, G. and Colin, J., 2017. Thermo-radiative simulation of an  
943 urban district with LASER/F. *Urban Climate*, 21: 43-65.

944 Krayenhoff, E.S., Christen, A., Martilli, A. and Oke, T.R., 2014. A Multi-layer Radiation  
945 Model for Urban Neighbourhoods with Trees. *Boundary-Layer Meteorology*,  
946 151(1): 139-178.

947 Krayenhoff, E.S. and Voogt, J., 2007. A microscale three-dimensional urban energy  
948 balance model for studying surface temperatures. *Boundary-Layer Meteorology*,  
949 123(3): 433-461.

950 Krayenhoff, E.S. and Voogt, J.A., 2016. Daytime Thermal Anisotropy of Urban  
951 Neighbourhoods: Morphological Causation. *Remote Sensing*, 8(2): 108.

952 Kusaka, H. and Kimura, F., 2004. Thermal Effects of Urban Canyon Structure on the  
953 Nocturnal Heat Island: Numerical Experiment Using a Mesoscale Model Coupled  
954 with an Urban Canopy Model. *Journal of Applied Meteorology*, 43(12): 1899-  
955 1910.

956 Lai, A., So, A.C., Ng, S. and Jonas, D., 2012. The Territory-Wide Airborne Light  
957 Detection and Ranging Survey for the Hong Kong Special Administrative Region,  
958 The 33RD Asian Conference on Remote Sensing, pp. 26-30.

959 Lee, D. et al., 2013. Modeling and observation of heat losses from buildings: The impact  
960 of geometric detail on 3D heat flux modeling.



961 Lemonsu, A., Grimmond, C.S.B. and Masson, V., 2004. Modeling the Surface Energy  
962 Balance of the Core of an Old Mediterranean City: Marseille. *Journal of Applied*  
963 *Meteorology*, 43(2): 312-327.

964 Li, Z.-L. et al., 2013. Satellite-derived land surface temperature: Current status and  
965 perspectives. *Remote Sensing of Environment*, 131: 14-37.

966 Martilli, A., Clappier, A. and Rotach, M.W., 2002. An Urban Surface Exchange  
967 Parameterisation for Mesoscale Models. *Boundary-Layer Meteorology*, 104(2):  
968 261-304.

969 Morrison, W. et al., 2018. A novel method to obtain three-dimensional urban surface  
970 temperature from ground-based thermography. *Remote Sensing of Environment*,  
971 215: 268-283.

972 Nazarian, N., Fan, J., Sin, T., Norford, L. and Kleissl, J., 2017. Predicting outdoor  
973 thermal comfort in urban environments: A 3D numerical model for standard  
974 effective temperature. *Urban Climate*, 20: 251-267.

975 Nazarian, N. and Kleissl, J., 2015. CFD simulation of an idealized urban environment:  
976 Thermal effects of geometrical characteristics and surface materials. *Urban*  
977 *Climate*, 12(0): 141-159.

978 Nazarian, N., Martilli, A. and Kleissl, J., 2018a. Impacts of Realistic Urban Heating, Part  
979 I: Spatial Variability of Mean Flow, Turbulent Exchange and Pollutant Dispersion.  
980 *Boundary-Layer Meteorology*, 166(3): 367-393.

981 Nazarian, N., Martilli, A., Norford, L. and Kleissl, J., 2018b. Impacts of Realistic Urban  
982 Heating. Part II: Air Quality and City Breathability. *Boundary-Layer Meteorology*.

983 Oke, T., 1988. The urban energy balance. *Progress in Physical geography*, 12(4): 471-508.

984 Peng, F., Wong, M.S., Ho, H.C., Nichol, J. and Chan, P.W., 2017. Reconstruction of  
985 historical datasets for analyzing spatiotemporal influence of built environment on  
986 urban microclimates across a compact city. *Building and Environment*, 123: 649-  
987 660.

988 Roth, M., Oke, T.R. and Emery, W.J., 1989. Satellite-derived urban heat islands from  
989 three coastal cities and the utilization of such data in urban climatology.  
990 *International Journal of Remote Sensing*, 10(11): 1699-1720.

991 Stewart, I.D., Oke, T.R. and Krayenhoff, E.S., 2014. Evaluation of the 'local climate  
992 zone' scheme using temperature observations and model simulations.  
993 *International Journal of Climatology*, 34(4): 1062-1080.

994 Voogt, J.A. and Oke, T.R., 1997. Complete urban surface temperatures. *Journal of*  
995 *Applied Meteorology*, 36(9): 1117-1132.

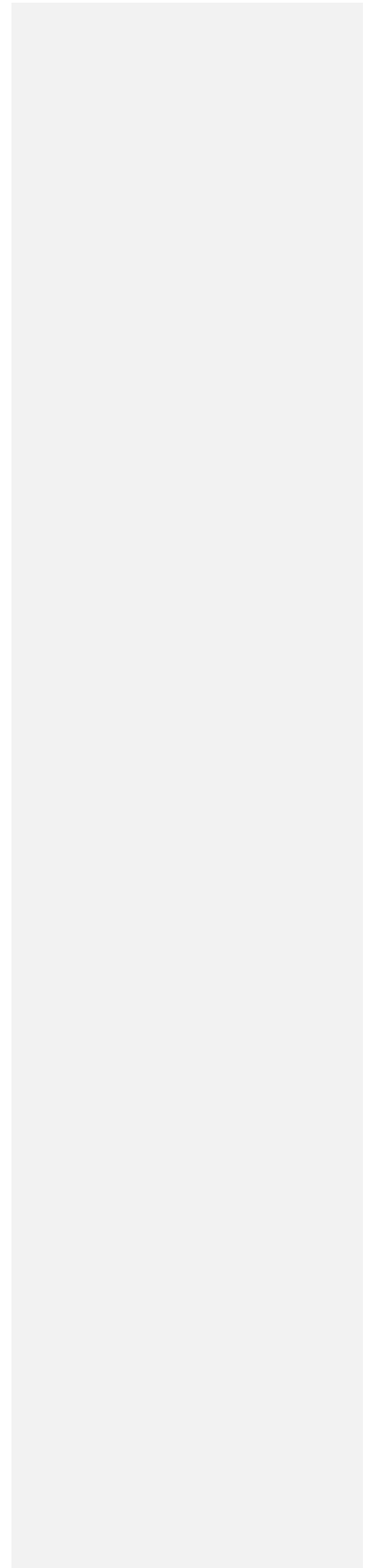
996 Voogt, J.A. and Oke, T.R., 2003. Thermal remote sensing of urban climates. *Remote*  
997 *sensing of environment*, 86(3): 370-384.

998 Wang, L. et al., 2014. Turbulent Transport of Momentum and Scalars Above an Urban  
999 Canopy. *Boundary-Layer Meteorology*, 150(3): 485-511.

1000 Weng, Q., 2009. Thermal infrared remote sensing for urban climate and environmental  
1001 studies: Methods, applications, and trends. *ISPRS Journal of Photogrammetry and*  
1002 *Remote Sensing*, 64(4): 335-344.

1003 Yaghoobian, N., Kleissl, J. and Krayenhoff, E.S., 2010. Modeling the Thermal Effects of  
1004 Artificial Turf on the Urban Environment. *Journal of Applied Meteorology and*  
1005 *Climatology*, 49(3): 332-345.

1006 Yang, J. et al., 2016. Development of an improved urban emissivity model based on sky  
1007 view factor for retrieving effective emissivity and surface temperature over urban  
1008 areas. *ISPRS Journal of Photogrammetry and Remote Sensing*, 122: 30-40.  
1009 Yang, X. and Li, Y., 2015. The impact of building density and building height  
1010 heterogeneity on average urban albedo and street surface temperature. *Building  
1011 and Environment*, 90(0): 146-156.  
1012



1013 **LIST OF FIGURE CAPTIONS**

1014 Figure 1. Study area: land uses in Kowloon peninsula and the Hong Kong Island.

1015 Figure 2. High spatial resolution thermal images acquired on Aug 5, 2013.

1016 Figure 3. Building heights of Kowloon peninsula and the Hong Kong Island.

1017 Figure 4. Relationships between the difference ( $T_c - T_r$ ) and  $\lambda_p$  under four different  
1018 daytime solar conditions.

1019 Figure 5. Relationship between the nighttime difference ( $T_c - T_r$ ) and  $\lambda_p$ .

1020 Figure 6. Relationship between the daytime difference ( $T_c - T_r$ ) and  $F$  under different  
1021 solar conditions.

1022 Figure 7. Relationship between the nighttime difference ( $T_c - T_r$ ) and  $F$ .

1023 Figure 8. Sensitivity of  $T_c - T_r$  to irradiance: a)  $T_c - T_r$  for cases 1 to 3 and; b) irradiance  
1024 cases 1 to 3 as applied in a).

1025 Figure 9. Sensitivity of  $T_c - T_r$  to wind speed under different conditions: a,  $\lambda_p=0.2$ ,  
1026  $H/L=2.5$ ; b,  $\lambda_p=0.2$ ,  $H/L=0.5$ .

1027 Figure 10. Impact of material properties on daytime  $T_c - T_r$ : ( $\max(T_c - T_r) - \min(T_c - T_r)$ )  
1028 obtained with the TUF – 3D numerical experiments and applying different combinations  
1029 of material properties in Table 2. (the parameter values applying to each experiment are  
1030 listed in the legend:  $H/L$  = ratio of building height to length;  $Kn$  = solar irradiance;  $\theta_a$  =  
1031 sun azimuth angle;  $\theta_z$  = sun zenith angle;  $\omega$  = wind speed)

1032 Figure 11. Impact of material properties on nighttime  $T_c - T_r$ : ( $\max(T_c - T_r) - \min(T_c - T_r)$ )  
1033 obtained with the TUF – 3D numerical experiments and applying different combinations  
1034 of material properties in Table 2. (the parameter values applying to each experiment are  
1035 listed in the legend:  $H/L$  = ratio of building height to length)

1036 Figure 12. Scatter plot between actual and estimated  $T_c$  in the process of determining the  
1037 coefficients: a,  $T_c$  from Eq. 8; b,  $T_c$  from Eq. 9.

1038 Figure 13. Comparison between  $T_c$  derived from  $T_r$  and  $T_c$  retrieved from component  
1039 temperatures based on high resolution airborne thermal images: a, on Aug 5, 2013; b, Oct  
1040 24, 2017.

1041 Figure 14. Radiometric,  $T_r$ , complete,  $T_c$ , surface temperature and their difference  $T_c - T_r$ ,  
1042 retrieved from Landsat TM Band 6 in 2010 based on Eq.8.

1043 Figure 15. Nighttime  $T_r$ ,  $T_c$  and their difference  $T_c - T_r$  retrieved from ASTER image data  
1044 in 2013 and GIS building based on Eq.9.

1045

1046